Statement: Please note that this article is a non-peer reviewed preprint submitted to EarthArXiv. Subsequent versions of this manuscript may have slightly different content. If accepted, the final version of this manuscript will be available via the 'Peer-reviewed Publication DOI' link on the right-hand side of this webpage.

Seasonal trends and drivers of land surface variables in Indo-Gangetic river basins

by Soner Uereyen[a], Felix Bachofer[a], Igor Klein[a], Claudia Kuenzer[a,b]

[a] German Remote Sensing Data Center (DFD), German Aerospace Center (DLR), Wessling, Germany

[b] Department of Remote Sensing, Institute of Geography and Geology, University Wuerzburg, Wuerzburg, Germany

Seasonal trends and drivers of land surface variables in Indo-Gangetic river basins

Soner Uereyen[a,*], Felix Bachofer[a], Igor Klein[a], Claudia Kuenzer[a,b]

[a] *German Remote Sensing Data Center (DFD), German Aerospace Center (DLR), Muenchener Strasse 20, 82234 Wessling, Germany*

[b] *Department of Remote Sensing, Institute of Geography and Geology, University Wuerzburg, Am Hubland, 97074 Wuerzburg, Germany*

Abstract

High mountain Asia holds the largest glacier mass on Earth outside the polar regions. In combination with monsoonal rainfall, glacial meltwater provides the downstream Indo-Gangetic river basins with indispensable water resources. These rivers supply 1.2 billion people with water and their water resources are essential for many sectors including the world's largest connected irrigated cropland and domestic needs. In this context, the quantification of land surface dynamics and driving factors is of particular interest to enhance the understanding of interplays between multiple spheres. This study investigates multivariate time series including climatic, hydrological, and remote sensing-based land surface and anthropogenic variables. For the first time, we generate dense time series of multiple remote sensing-based land surface variables at biweekly intervals and employ statistical time series analyses at seasonal and annual scale. We analyze trends and controlling variables in consideration of temporal lags using causal networks between December 2002 and November 2020. The results show increasing trends in vegetation greenness being accelerated during the second half of the study period. Furthermore, a mismatch between trends in surface water area and terrestrial water storage was identified. Considering snow cover area, trends remain mostly insignificant at basin scale suggesting no change during the 18 years. At seasonal and grid scale, analyses indicate negative trends over the Upper Ganges and Brahmaputra river basins particularly during the monsoon and post-monsoon season. Furthermore, the causal networks revealed so far unexplored interactions among multivariate feature spaces at seasonal scale. For example, vegetation greenness is constrained by water availability, surface water area is influenced by river discharge, snow cover, and temperature, whereas snow cover area is largely controlled by precipitation and temperature with spatial and temporal variations. To summarize, these findings provide valuable insights with respect to the trends and interactions between various spheres in the Indo-Gangetic river basins.

Keywords: Remote sensing, MODIS time series, Climatic controls, Anthropogenic influence, Himalaya Karakoram, South Asia

*Corresponding author

Email address: soner.uereyen@dlr.de (Soner Uereyen)

1. Introduction

In times of amplified global climate change, river basins originating at the Himalaya-Karakoram are facing increasing environmental and human pressure (Song et al., 2018; Wijngaard et al., 2018). The Indus, Ganges, Brahmaputra, and Meghna rivers represent in combination one of the largest transboundary river basins worldwide supplying about 1.2 billion people (Table S1, Lloyd et al. 2019) with water resources, where irrigated agriculture is of particular importance (Biemans et al., 2019). The main contributors to water resources in these river basins are meltwater from glaciers and snow as well as monsoon rainfall (Pritchard, 2019; Viviroli et al., 2020). Over the last decades, terrestrial water storage declined in the Indus and Ganges plains and was linked to unsustainable water withdrawal (MacDonald et al., 2016). In this context, increasing temperature influenced the snow cover and glacier mass over high altitude areas (Miles et al., 2021; Pepin et al., 2015). Moreover, it was found that the spatial pattern and intensity of monsoon rainfall will likely change in the long term and have negative impacts on water resources (Hasson et al., 2017; Mondal et al., 2021). Additional findings support the assumption that the occurrence of extreme events such as droughts and heatwaves (Dangar and Mishra, 2021; Mishra et al., 2020) or flooding (Nie et al., 2021) will intensify and impact future characteristics of the land surface, societies, and economies of the Indo-Gangetic river basins.

To enhance the understanding of seasonal land surface dynamics and the influence of climatic, hydrological, and anthropogenic factors in the Indo-Gangetic river basins, holistic time series analyses are required. In this connection, satellite-based Earth observation (EO) provides essential information on several land surface variables over large areas, including characteristics on vegetation, surface water, snow cover, as well as land cover and land use (Mahecha et al., 2020; Uereyen and Kuenzer, 2019; Woodcock et al., 2020). For example, satellite imagery of the Moderate Resolution Imaging Spectroradiometer (MODIS) sensors provide consistent data in terms of spatial and temporal coverage since the year 2000. These observational data enable comprehensive analyses of trends over the last decades. In addition, a combination of land surface variables with geospatial climatic and hydrological time series allow the analysis of interdependencies within a multivariate feature space. Although numerous studies investigated trends of single land surface variables including the normalized difference vegetation index (NDVI) or leaf area index (LAI) (Chen et al., 2019; Mishra and Mainali, 2017) and snow cover area (SCA) (Notarnicola, 2020; Wang et al., 2017), the consistent exploration of multiple land surface variables at seasonal and annual temporal scale as well as at various spatial scales is yet rarely performed. Furthermore, evaluation of driving variables is often conducted by means of correlation (e.g. Lamchin et al. 2018), partial correlation (e.g. Liu et al. 2021), or residual analysis (e.g. Zheng et al. 2019). Recently, Runge et al. (2019) proposed a causal discovery algorithm named Peter and Clark Momentary Conditional Independence (PCMCI). Compared to traditional approaches, PCMCI is capable of handling a high dimensional feature space, highly autocorrelated data, and allows the quantification of direct and indirect influences.

In this study, we create a high dimensional feature space consisting of geospatial time series covering multiple spheres at biweekly temporal resolution. To this end, we use EO-based time series on NDVI, surface water area (SWA), and SCA in combination with climatic, hydrological, and anthropogenic time series for Indo-Gangetic river basins during the period December 2002 to November 2020. Specifically, the objectives of our study are (1) to estimate seasonal and annual trends at grid and basin scale, (2) to quantify direct and indirect influences on land surface variables at seasonal scale, (3) to assess and evaluate human influence on land surface parameters, and (4) to explore spatial variations in seasonal trends and driving variables of land surface parameters.

2. Materials and methods

2.1. Study area

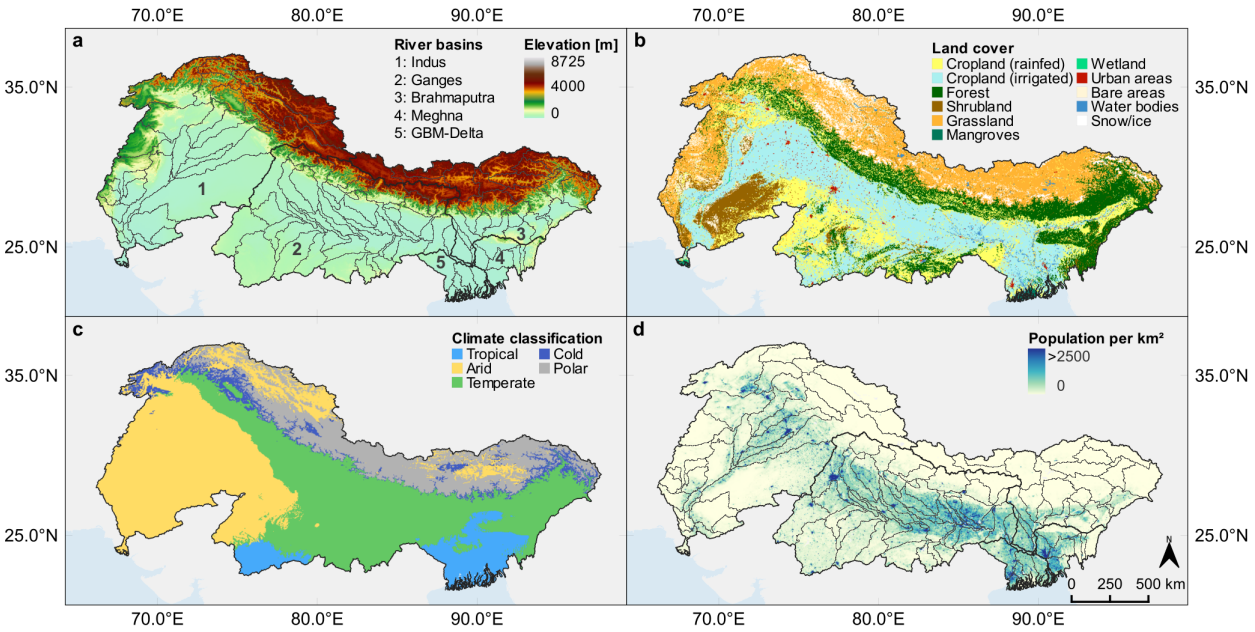

Figure 1: Characteristics of the study area showing (a) Copernicus Digital Elevation Model (DEM) (Airbus, 2020) and outlines of the large river basins and subbasins with light gray boundaries extracted from HydroSHED (Lehner et al., 2008), (b) reclassified land cover classes for 2019 provided by the European Space Agencies (ESA) Climate Change Initiative (CCI) (European Space Agency and Sinergise, 2021), (c) climate zones extracted from Köppen-Geiger classification (Beck et al., 2018), and (d) gridded population counts from WorldPop population data at 1 km spatial resolution (Lloyd et al., 2019).

The Indus-Ganges-Brahmaputra-Meghna river basins cover an area of approximately 2.8 million km^2 (Table S1) and are located in South Asia. These transboundary river basins include the countries Afghanistan, Pakistan, India, China, Nepal, Bhutan, and Bangladesh. In this study, the Ganges-Brahmaputra-Meghna

(GBM) Delta is considered as a separate spatial entity. The upstream regions of these basins are characterized by high mountain regions including the Himalaya-Karakoram mountain ranges with cold and polar climate (Azam et al., 2021), whereas the downstream basins include the Indo-Gangetic plains being characterized by low altitudes, intensive agriculture with largely irrigated areas (Biemans et al., 2019), and dense population (Fig. 1). In total, these river basins inhabit approximately 1.2 billion people (Table S1, Lloyd et al. 2019) and include a number of mega cities such as Lahore, New Delhi, Kolkata, and Dhaka highlighting its social and economic importance. Moreover, the climate in the downstream basins is arid in western parts and temperate as well as tropical in central and eastern regions of the basins. In these basins, water supply is primarily modulated by snow and glacier melt, groundwater, and monsoon rainfall (Biemans et al., 2019; Viviroli et al., 2020). The southwest monsoon causes extreme rainfall events being highest north of the Bay of Bengal between June and September. Likewise, the northeast monsoon induces high rainfall over the Karakoram mountains in the northwest of the study area during the winter months between December and February. While the Karakoram receives less annual rainfall than the Himalayan region, the northeast monsoon leads to more extensive snow cover in the Karakoram (Azam et al., 2021).

2.2. Time series data

We utilized several geospatial time series variables characterizing land surface, climatic, hydrological, and anthropogenic features for the period between December 2002 to 2020. To this end, all used variables were available at daily temporal resolution. For further analyses, we aggregated the time series to biweekly temporal intervals. To incorporate time series at annual temporal resolution, in particular the anthropogenic time series, we additionally aggregated biweekly time series to annual scale.

2.2.1. Vegetation

In this study, we used daily Terra and Aqua MODIS (M*D09GA.006) surface reflectance products at 500 m spatial resolution to derive the NDVI. The study period was selected in consideration of the overlapping period of both sensors, to guarantee consistent and high quality observations. To obtain the highest quality MODIS NDVI observations, quality flags were applied to exclude pixels contaminated by snow, cloud cover, and shadow. Since the quality assurance layers are provided at 1 km spatial resolution, the daily surface reflectance products were spatially aggregated during application of quality flags from 500 m to 1 km. Furthermore, daily Terra and Aqua MODIS time series were temporally aggregated to biweekly time steps by considering the median observation in order to reduce the influence of extreme values, respectively. In the following step, observations of both sensors were combined by calculating the average for the respective biweekly period. Remaining gaps in the biweekly NDVI time series were filled using linear interpolation. Moreover, to exclude non-vegetated areas, all NDVI pixels with a long-term mean lower than 0.15 were masked out as suggested by Wittich and Hansing (1995).

2.2.2. Snow cover area

The Global SnowPack (GSP) is processed at the German Aerospace Center (DLR) and is used to perform analyses on SCA changes (Dietz et al., 2015). We employ GSP, as it is based on daily MODIS (M*D10A1.006) snow products at a spatial resolution of 500 m and thus, enables aggregation to biweekly intervals. In this context, MODIS snow data are widely used to characterize changes in snow cover (Nepal et al., 2021; Notarnicola, 2020; Rößler et al., 2021). Dietz et al. (2015) implemented several processing steps to interpolate pixels obscured by cloud coverage. To reduce further uncertainties related to cloud cover and ephemeral snow, we masked snow pixels at an elevation lower than 1500 m using the Copernicus Digital Elevation Model (DEM) at 90 m spatial resolution (Airbus, 2020). Moreover, we excluded all pixels with a long-term mean lower than 10 % and being outside the cold and polar climate zone at the same time.

2.2.3. Surface water area

We use both, daily DLR Global WaterPack (GWP) (Klein et al., 2017, 2021) and monthly Global Surface Water Layer (GSWL) v1.3 developed at the Joint Research Centre (JRC) (Pekel et al., 2016) to analyze SWA dynamics. While GWP is based on daily MODIS (M*D09GQ.006) data at 250 m spatial resolution, the Landsat archive is used to map GSWL at 30 m spatial resolution. Using these datasets together enables exploitation of their respective advantages being daily temporal resolution for GWP and high spatial resolution of GSWL. Despite the high temporal resolution, GWP might underestimate inland water bodies or river streams due to, e.g., coarse resolution and mixed pixels or high sediment load which impacts the water color. We aimed to alleviate these underestimations by using both datasets complementary. The GSWL was downloaded through the Google Earth Engine (Gorelick et al., 2017) and aggregated to the spatial resolution of GWP. Then, we temporally aggregated daily to biweekly GWP. For pixels of biweekly GWP composites being labeled with "no water" and GSWL labeled with "water" for the respective time step, the value of GSWL was inherited.

2.2.4. Climatic and hydrological variables

For analysis of climatic and hydrological controls on the land surface, we used ERA5-Land reanalysis data from the European Centre for Medium-Range Weather Forecasts (ECMWF) (Muñoz-Sabater, 2019). ERA5-Land is the enhanced land component of the ERA5 reanalysis product comprising hourly atmospheric, land, and oceanic meteorological variables since 1950 at a spatial resolution of approximately 9 km. Due to the hourly temporal resolution, this dataset particularly fits the aim of this study to generate time series at bi-weekly intervals. Lately, ERA5-Land data has been widely used for studies covering the Indo-Gangetic Plains and Himalayan region (Bhattacharya et al., 2021; Kolluru et al., 2020; Mishra et al., 2020; Nepal et al., 2021). In detail, we extracted accumulated daily precipitation and surface solar radiation downward from the hourly data. Additionally, hourly 2-m air temperature, soil moisture (7 – 28 cm), and 2-m dewpoint temperature was averaged to daily temporal scale. Based on temperature and dewpoint temperature, the vapor pressure

deficit based on the formula in Barkhordarian et al. (2019) was calculated. ERA5-Land temperature trends and anomalies indicate good agreement with in-situ observations in the Himalayan region (Bhattacharya et al., 2021) and India (Mishra et al., 2020). However, one has to keep in mind that validation of gridded reanalysis data remains a challenge due to sparse network of weather stations, particularly in the Himalayan region (Bhattacharya et al., 2021). Kolluru et al. (2020) demonstrated that daily ERA5 precipitation data performs well over selected basins in India. Nepal et al. (2021) also reported that the precipitation data matches the seasonal variability. Regarding solar radiation, studies indicated good performance of ERA5 compared to other datasets (Urraca et al., 2018; Yang and Bright, 2020). On the other hand, evaluation of ERA5 soil moisture with in-situ measurements reflected good agreement and superiority compared to other reanalyses data (Li et al., 2020). Additionally, we also utilized GloFAS-ERA5 gridded global river discharge v3.1 data (Harrigan et al., 2020) as indicator for river discharge observations. To date, this dataset has not been comprehensively validated over the investigated river basins. However, Harrigan et al. (2020) reported good performance compared with globally distributed observations. Finally, to quantify changes in terrestrial water storage anomaly (TWSA), we use a daily dataset based on the Gravity Recovery And Climate Experiment (GRACE) mission generated at the Institute of Geodesy at Graz University of Technology (ITSG) (Kvas et al., 2019; Mayer-Gürr et al., 2018). However, the availability of the TWSA data is only covering the period 2003–2016.

2.2.5. Indicators for human impact

We obtained several datasets as indicator for anthropogenic forcing in our study area. These include the ESA CCI land cover (300 m) (European Space Agency and Sinergise, 2021), gridded population data (1 km) (Lloyd et al., 2019), harmonized nighttime lights (1 km) from Li and Zhou (2017), and the World Settlement Footprint (WSF) layer, which characterizes the change in the extent of settlement areas (Marconcini et al., 2020). The WSF Evolution covers the period 1985–2015 (Marconcini et al., 2021). These datasets are provided at annual temporal resolution. Furthermore, to differentiate NDVI for several vegetation classes, we use land cover data to extract stable pixels for the classes forest, grassland, irrigated cropland, and rainfed cropland being consistent over the studied period. Afterwards, we aggregate the extracted four classes to the spatial resolution of the NDVI data (1 km) and intersect the NDVI layer with the respective class.

2.3. Methods

2.3.1. Time series harmonization

Following the preprocessing of the univariate time series variables, all datasets were harmonized to a common spatial unit by averaging. This step enables joint analyses of all variables (Fig. 2). For this study, grids at a spatial resolution of 0.01° and the outlines of the large river basins and respective subbasins were used to unify the geospatial time series (Fig. 1).

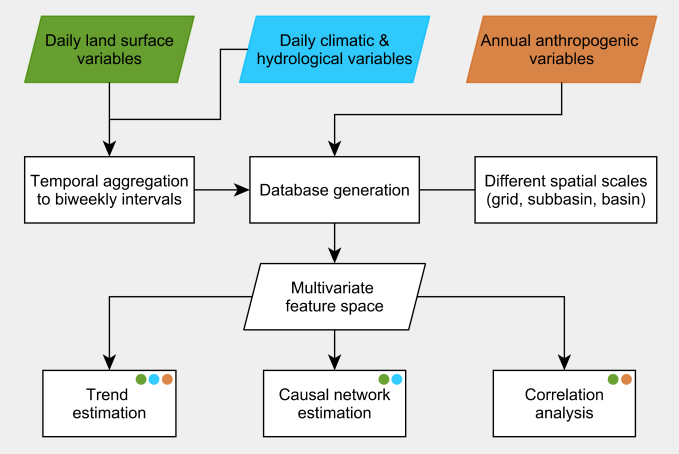

Figure 2: Simplified overview of applied methodological framework to generate a multivariate feature space and apply statistical time series analysis techniques.

2.3.2. Trend estimation

The widely used non-parametric Mann-Kendall test in combination with the Theil-Sen slope estimator was employed for trend estimation. If serial correlation at lag-1 is statistically significant for the time series at a confidence level of 95 %, we first applied prewhitening and then derived the trend metrics. As suggested in literature, our analysis did not rely on only one prewhitening approach (Collaud Coen et al., 2020; Wang et al., 2015). To assess the statistical significance of the trend, the trendfree prewhitening algorithm after Wang and Swail (2001) was utilized. Furthermore, the estimation of the magnitude of the trend, was based on the variance correction prewhitening approach after Wang et al. (2015). Ultimately, the trend tests were performed at seasonal as well as annual scale. For this purpose, we first calculated trend metrics at seasonal scale for the period December 2002 to November 2020. During this step, the biweekly temporal resolution was kept, which results in a higher number of data points enhancing the power of the trend tests (Collaud Coen et al., 2020). Next, based on the seasonal trends, the annual trend was estimated. At seasonal scale we considered following meteorological seasons: winter (DJF), pre-monsoon (MAM), monsoon (JJAS), and post-monsoon (ON) (Janes et al., 2019). Ultimately, trends are only considered, if they are statistically significant at a confidence level of 95 %. In case of an insignificant trend, we consider it as a tendency. Furthermore, all presented trend values are calculated at decadal scale by multiplying the respective slope value with the number of years per decade.

2.3.3. Causal network estimation

To explore contemporaneous (lag 0) and lagged dependencies within a set of univariate time series variables, we used an extended version of the PCMCI algorithm, specifically PCMCI$^+$ (Runge et al., 2019; Runge, 2020). The causal discovery algorithm PCMCI$^+$ constructs causal networks, where the nodes depict the present variables and the edges the presence and direction of the detected causal relation among the

variables. PCMCI employs a two-step procedure to identify linear or non-linear causal links. First, a version of the Peter and Clark (PC) algorithm is applied to extract potential time lagged parents for each input variable. Second, the momentary conditional independence (MCI) test is applied using a conditional independence test. In this study, we applied the linear partial correlation option. During the MCI step, causal links between the variables are tested given the discovered potential parents of the tested variables derived in the first step. Using standard PCMCI, contemporaneous links are tested during the second step as well. However, the causal direction is left undirected since a temporal order is not available for instantaneous links. Though, in PCMCI$^+$ the algorithm is extended being also capable of detecting directed contemporaneous links (Runge, 2020).

In our study, we created a unique feature space for each of the land surface variable NDVI, SWA, and SCA including relevant driving variables, respectively. During causal analysis, only time series at biweekly temporal resolution were utilized. This might enhance the detection of causal links, which could potentially disappear at a temporal resolution of e.g. one month. Moreover, we set a maximum time lag of three months corresponding to six-time steps at biweekly scale. In order to meet the stationarity requirement for time series when adopting partial correlation as independence test, the linear trend of the time series was removed by least square fit and then seasonal anomalies were calculated (Runge et al., 2019). With respect to the fulfillment of the causal stationarity assumption, the mask option within the PCMCI framework was employed in addition. In particular, the time series were split to the aforementioned meteorological seasons. In case of NDVI, the time series was additionally limited to the growing season using only values with an NDVI lower than 0.2 and temperature lower than 0°C as suggested by (Wu et al., 2015). Further details on employed settings are listed in Table S2. Moreover, we quantified indirect influences on the land surface variables NDVI, SWA, and SCA at subbasin scale. In this context, we first spatially intersected all driving variables with the respective land surface variable and then computed causal graphs. The intersection step excluded i.e. non-vegetated areas for all of the considered variables from the analysis. Lastly, one has to note that causal analysis requires that all relevant variables in a specific system are accounted for (Runge et al., 2019). Therefore, the presented results and interpretations are only valid with respect to the created feature space, since modifying the feature space could change the resulting causal graphs (Di Capua et al., 2020).

2.3.4. Analysis of human forcing

Aiming at evaluating human influence on land surface variables, NDVI trends for several vegetation classes (section 2.2.5) are further analyzed. Moreover, we also quantify the relationship between NDVI and SWA with available geospatial data on human influence within the study area. These include annual time series of population, nighttime lights, and settlement area. To accomplish this objective, we used the annual trends of respective variables at subbasin scale and calculated the Pearson correlation coefficient to assess the relationship.

3. Results

3.1. Trends of environmental variables

Table 1 summarizes trends of the land surface, climatic, and hydrological variables at basin and seasonal as well annual scale, respectively. Considering NDVI, significant trends are all positive at seasonal and annual scale. At seasonal scale the magnitude of trends is highest during winter months in the Indus and Ganges river basins, whereas the Brahmaputra, Meghna, and GBM-Delta have the highest trend value during the pre-monsoon season. All significant trends in SWA also indicate a positive direction. Partially negative tendencies for SWA can be observed for a number of seasons with insignificant results in the Indus, Brahmaputra, and Meghna river basins. In contrast, significant trends of TWSA indicate declining groundwater at annual scale for all of the basins. At basin scale, SCA barely shows significant trends. Significant negative trends are only present for the Ganges and Brahmaputra river basins in the monsoon and post-monsoon season, respectively. Furthermore, Fig. 3 demonstrates the time series at annual scale (Fig. S1). It becomes evident, that NDVI shows a clear increasing tendency, particularly since 2018 for the GBM-Delta and Indus as well as Ganges river basins. Considering the anomalies in SWA, there is a clear relationship with precipitation for the GBM-Delta and Meghna river basin (Fig. 3b,d). Additionally, it is likely that anomalies in precipitation and temperature influence SCA. For example in 2016, SCA reaches its lowest value in the Indus river basin (Fig. 3c). At the same time, temperature shows a positive and precipitation a negative anomaly (Fig. 3d,e).

Moreover, Fig. 4 shows seasonal trends of the land surface parameters NDVI, SWA, and SCA at grid scale. For the studied period, NDVI indicates significant positive trends during the winter and pre-monsoon season for 68.4 % and 65.0 % of the grids, respectively (Fig. 4a). These are particularly pronounced in the central Indus and southwest Ganges river basin (DJF) as well as north of the Bay of Bengal (MAM). The post-monsoon season is characterized by a large number of insignificant trend values (67.5 %) and the highest share of significant negative trends (2.8 %). With respect to the seasonal trends in SWA, the results indicate a largely significant positive direction (Fig. 4b), e.g. during the pre-monsoon season 40.5 % and 7.0 % of the grids imply significant positive and negative trends, respectively. Significant negative trends are dominant along the Brahmaputra river in the downstream region of the Himalaya (DJF, MAM), at the wetlands in the Meghna river basin (JJAS, ON), at the confluence of the Ganges and Brahmaputra (JJAS, ON), and in the GBM-Delta (DJF, MAM). Regarding the entire study area, the highest amount of significant negative trends occurs in winter (11.1 %). Furthermore, results of the trend analysis for SCA point towards no change in the Indus river basin (Fig. 4c). In comparison, in the Ganges and Brahmaputra river basins, SCA shows significant positive trends during the pre-monsoon season, while we identified significant negative trends during the monsoon (10.2 %) and post-monsoon season (14.3 %).

3.2. Drivers of land surface variables

Fig. 5 demonstrates direct drivers of the land surface variables having the highest influence per grid at seasonal scale. In regards of NDVI, soil moisture has the highest influence throughout the seasons (Fig. 5a,

Table 1: Annual and seasonal trends at basin scale for the period between December 2002 and November 2020. Variables include NDVI, SWA, SCA, precipitation (P), terrestrial water storage anomaly (TWSA), temperature (T), surface solar radiation downward (DSR), river discharge (Q), soil moisture (SM), and vapor pressure deficit (VPD). All trend values are computed at decadal scale and the percent values are relative to the respective basin area. Bold values represent statistically significant trends (p-value < 0.05).

Basin	Season	NDVI	SWA [%]	SCA [%]	P [mm]	TWSA [cm]	T [°C]	DSR [W m^{-2}]	Q [mm^{-3} s^{-1}]	SM [m^3 m^{-3}]	VPD [kPa]
Ganges	DJF	**0.055**	**0.034**	0.233	**2.608**	**−6.804**	**−0.333**	**−3.270**	**2.439**	**0.003**	**−0.058**
	MAM	**0.039**	**0.095**	0.474	**3.370**	**−1.532**	**−0.469**	**−5.761**	**3.009**	**0.005**	**−0.143**
	JJAS	**0.028**	0.046	**−0.218**	7.235	**−5.903**	0.241	−6.524	48.436	0.002	−0.032
	ON	0.007	**0.105**	−0.360	−1.082	**−4.684**	0.443	−3.113	−0.626	−0.005	−0.006
	Annual	**0.034**	**0.071**	0.008	**2.989**	**−5.293**	−0.046	**−4.516**	**2.724**	0.002	**-0.045**
Brahmaputra	DJF	**0.015**	−0.012	−0.319	0.971	**−7.467**	0.027	−1.016	0.614	**−0.003**	−0.002
	MAM	**0.021**	−0.017	0.995	−2.030	**−11.501**	−0.272	−1.614	−12.928	0.001	−0.013
	JJAS	**0.008**	**0.115**	−0.302	11.523	**−12.173**	**0.375**	**−9.165**	45.747	0.003	−0.003
	ON	**0.014**	**0.050**	**−1.350**	1.009	**−11.025**	0.748	0.293	11.032	−0.002	0.012
	Annual	**0.014**	0.019	−0.310	0.990	**−11.263**	−0.046	**−1.315**	5.823	0.000	−0.003
Meghna	DJF	**0.025**	0.536	-	1.196	−1.115	−0.149	−4.776	1.247	0.003	**−0.053**
	MAM	**0.043**	0.302	-	4.839	**−3.497**	−0.231	−3.110	4.918	0.007	−0.024
	JJAS	**0.027**	−0.630	-	−6.022	**−3.036**	**0.353**	−2.507	0.577	**−0.003**	0.024
	ON	**0.015**	−0.138	-	1.332	**−3.375**	0.154	−3.930	2.559	0.006	−0.019
	Annual	**0.026**	0.082	-	1.264	**−3.206**	0.003	−3.520	1.903	0.005	−0.022
Indus	DJF	**0.048**	−0.086	−0.600	−2.321	**−4.181**	−0.332	2.598	−0.586	−0.001	0.000
	MAM	**0.040**	**0.092**	0.075	**3.934**	**3.292**	−0.425	**−7.101**	**13.909**	**0.009**	**−0.152**
	JJAS	**0.041**	**0.166**	−0.265	−0.017	**−2.530**	0.293	−2.072	6.224	0.000	0.014
	ON	0.016	0.056	0.603	1.724	2.233	0.051	−3.914	−0.551	0.005	−0.043
	Annual	**0.040**	**0.074**	0.007	0.853	**−0.149**	−0.141	−2.993	2.836	0.002	−0.021
GBM-Delta	DJF	**0.034**	**0.466**	-	1.110	**−4.959**	−0.125	**−8.465**	3.023	0.004	**−0.068**
	MAM	**0.050**	−0.054	-	8.919	**−6.338**	−0.529	−7.694	0.720	**0.012**	**−0.096**
	JJAS	**0.035**	**0.384**	-	−0.342	**−6.692**	**0.368**	5.019	61.325	−0.003	0.031
	ON	0.019	**0.429**	-	1.298	**−4.622**	0.201	−2.389	14.483	0.004	−0.012
	Annual	**0.034**	**0.407**	-	1.204	**−5.648**	0.038	−5.041	8.753	0.004	−0.040

Fig. S2). Particularly in the pre-monsoon season, 34 % of the grids are influenced most by soil moisture. During winter season, temperature appears to be the dominant controlling factor in the upper Indus plains. Vapor pressure deficit appears to be strongly linked with NDVI in the northeast of the Brahmaputra river basin and during the monsoon in the Indo-Gangetic plain. In addition, it is striking that in high altitudes of the Brahmaputra river basin, water availability through soil moisture is an important factor for vegetation condition during the monsoon season. Furthermore, it is noticeable that grids with no significant causal link between NDVI and its drivers are mostly present in parts of the Indo-Gangetic plain. Considering the temporal lags between NDVI and driving variables, highest effect size is mostly reached at lag 1 followed by lag 0 (Fig. S3). Next, PCMCI$^+$ implies that SWA is strongly controlled by river discharge throughout the seasons, whereas at high altitudes, SCA and temperature are an important driving factor as well (Fig. 5b, Fig. S4). In case of SWA, the strongest links are present at lag 0, but in the monsoon season at lag 1 (Fig. S5). Regarding direct drivers of SCA, the occurrence of temperature is striking, particularly during the monsoon season over the upper Indus basin (Fig. 5c, Fig. S6). Precipitation appears to affect SCA largely over the winter season, while being less important in the pre-monsoon and post-monsoon season. Moreover,

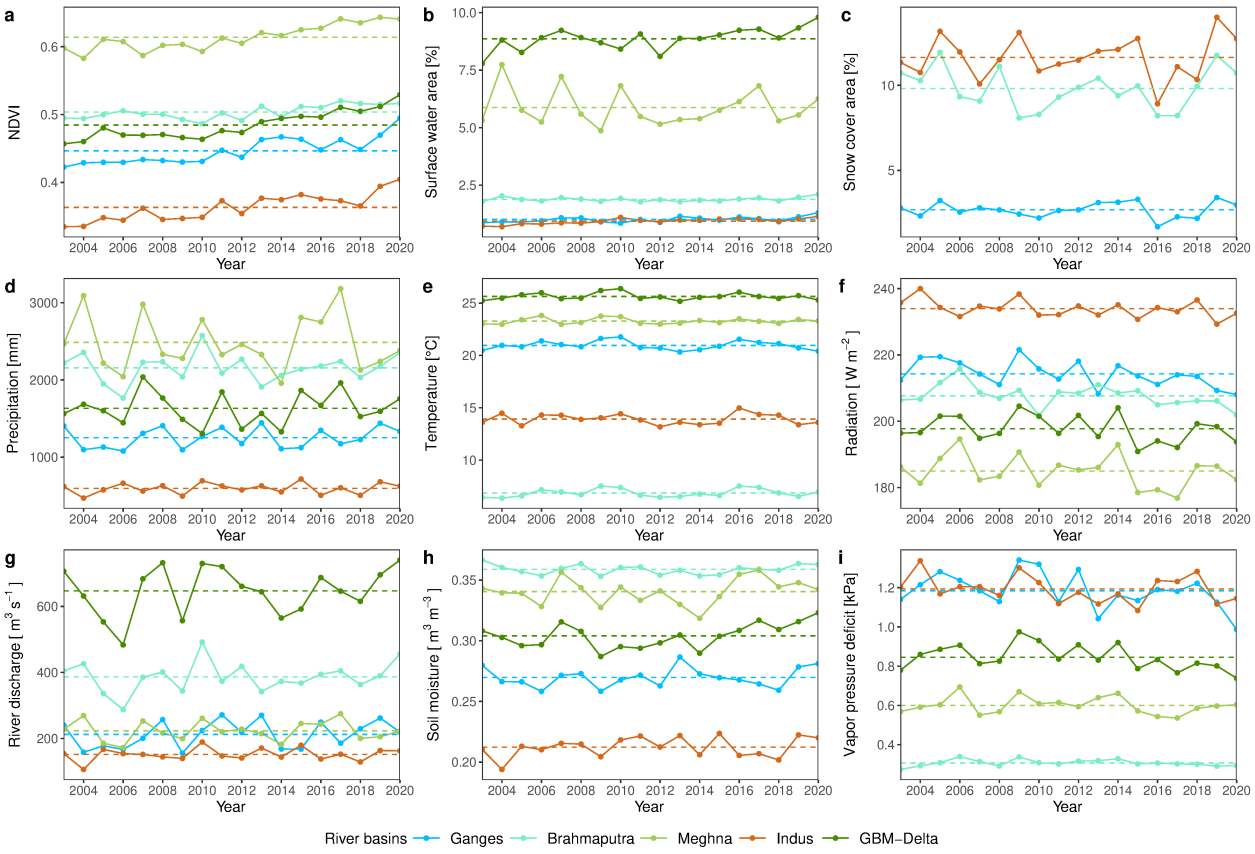

Figure 3: Time series variables for the river basins at annual scale covering the period between 2003 and 2020. The dashed line represents the respective average value of the time series.

temperature controls SCA instantaneously, but precipitation with a lag of 1 (Fig. S7).

3.3. Indirect influences on land surface variables

Besides assessing direct influences on the land surface parameters, we estimated the relation between all variables of interest to additionally quantify indirect links. Fig. 6 demonstrates the causal process graphs at seasonal scale. Considering the graphs, it is visible that the identified causal links are changing over the seasons. In case of the feature space including NDVI, the causal links between precipitation and soil moisture are dominant over all seasons (Fig. 6a). A direct link between soil moisture and NDVI occurs over the pre-monsoon and monsoon season, while an indirect link is present for the post-monsoon season via vapor pressure deficit. Furthermore, NDVI is directly positively controlled by precipitation over all seasons except for the pre-monsoon season. Here, an indirect connection exists between NDVI and precipitation via soil moisture. In addition, PCMCI$^+$ unveils a negative influence of radiation and vapor pressure deficit on NDVI for almost all seasons. Further on, while temperature is directly influencing NDVI positively in winter, this connection turns negative during the other seasons via indirect paths. On the other hand, SWA is directly and positively controlled by both precipitation and river discharge (Fig. 6b). In fact, during the winter, monsoon, and post-

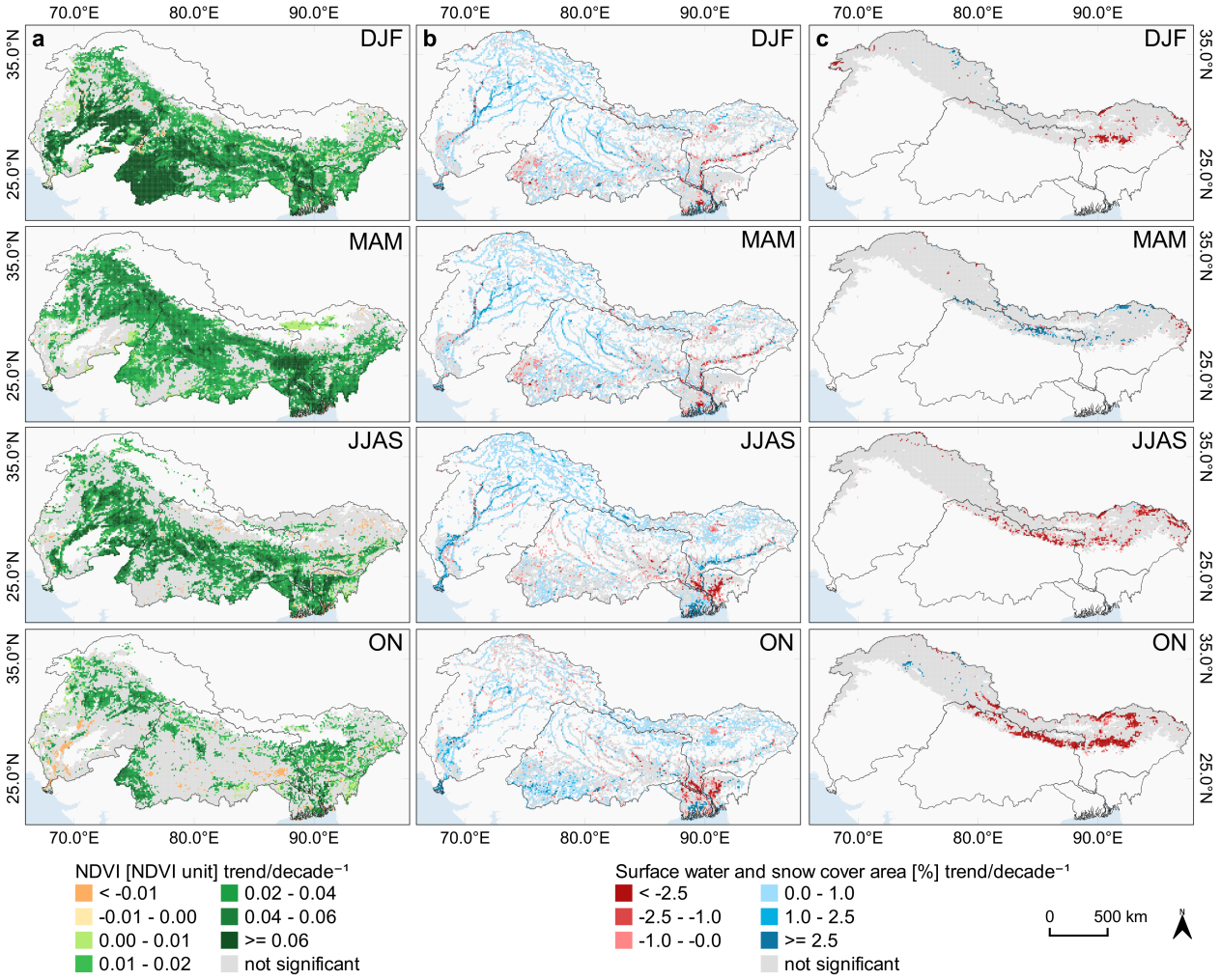

Figure 4: Seasonal trends for (a) NDVI, (b) SWA, and (c) SCA covering the period between December 2002 and November 2020. We divided the biweekly time series into the meteorological seasons DJF, MAM, JJAS, and ON. Grids outside the 95 % confidence level are colored in gray.

monsoon season precipitation also has an indirect path towards SWA via river discharge. On the contrary, SWA is negatively influenced by radiation through direct and indirect links via river discharge. Regarding the feature space including SCA, most variables appear to be connected contemporaneously (Fig. 6c). In general, precipitation controls SCA positively at a temporal lag of 1 and during the monsoon season at lag 0. In addition, radiation and temperature are coupled negatively to SCA. However, in the post-monsoon season SCA influences temperature negatively.

3.4. Human forcing on land surface variables

Table 2 lists seasonal and annual trends for NDVI stratified by land cover classes at basin scale. It becomes evident, that rainfed and irrigated croplands are the main driver of the vegetation greening. At annual scale the significant trends are highest for irrigated croplands for all basins. In comparison, at seasonal

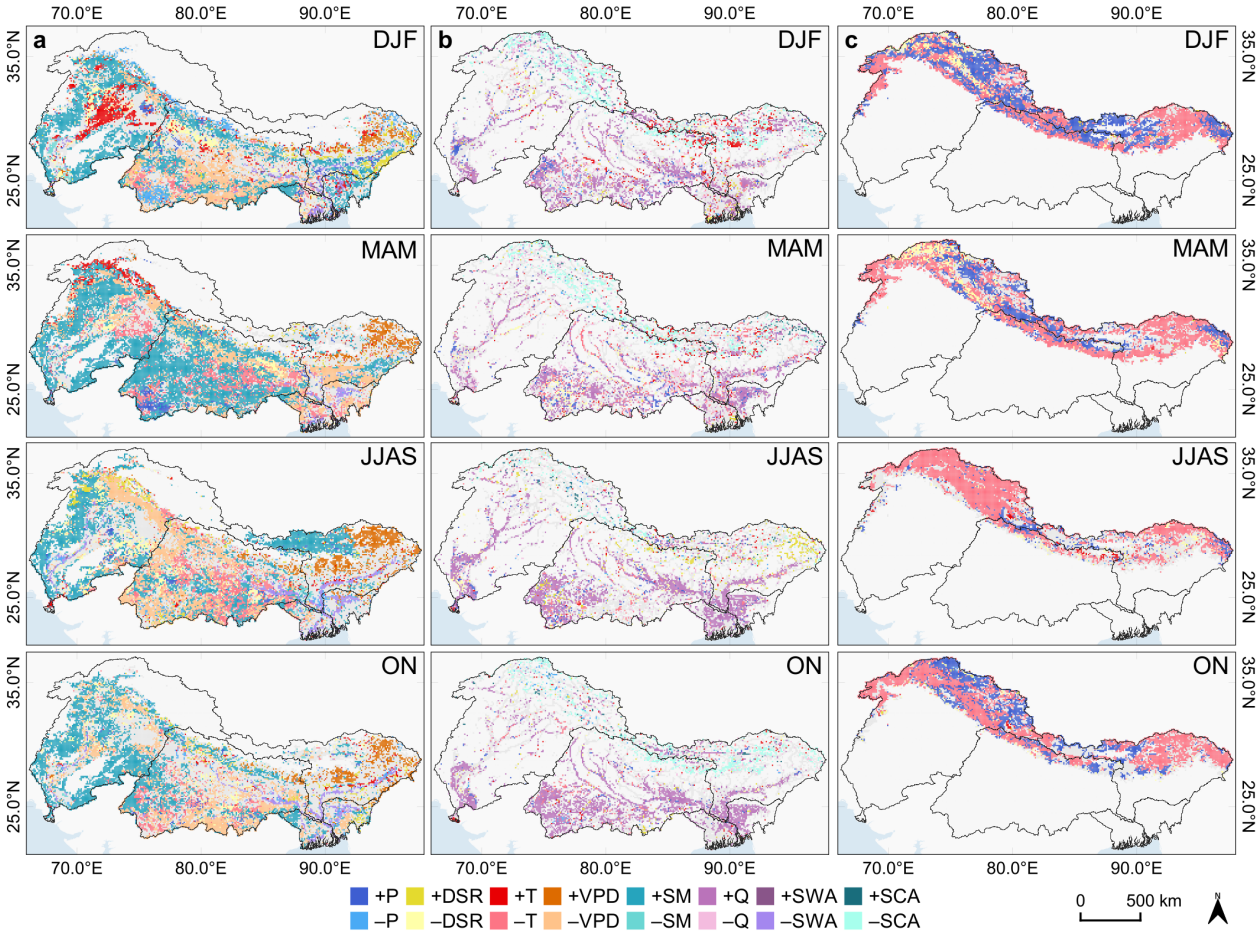

Figure 5: Driving variables with highest effect size per season for (a) NDVI, (b) SWA, and (c) SCA. To estimate causal networks, the biweekly time series are divided into the meteorological seasons DJF, MAM, JJAS, and ON. The driving variables include precipitation (P), soil moisture (SM), temperature (T), surface solar radiation downward (DSR), vapor pressure deficit (VPD), river discharge (Q), SWA, and SCA. Grids with gray color indicate no causal link between target and driving variables. Feature space of (a) NDVI: P, DSR, T, VPD, SM, SWA; (b) SWA: P, DSR, T, Q, SCA; (c) SCA: P, DSR, T.

scale trends are particularly high for irrigated areas during the winter and pre-monsoon season for the Ganges, Brahmaputra, and Indus river basins.

Fig. 7 illustrates the correlation between trend values of land surface and anthropogenic variables. Here, the correlation between NDVI and anthropogenic factors are all positive (Fig. 7a–c). For example, the scatterplots indicate that NDVI trends are particularly high in subbasins with increasing settlement area. On the contrary, the correlation of trends in SWA and anthropogenic factors is negative (Fig. 7d–f). The relation implies that increase in SWA occurs in subbasins, where i.e. increase in settlement area and population is lowest.

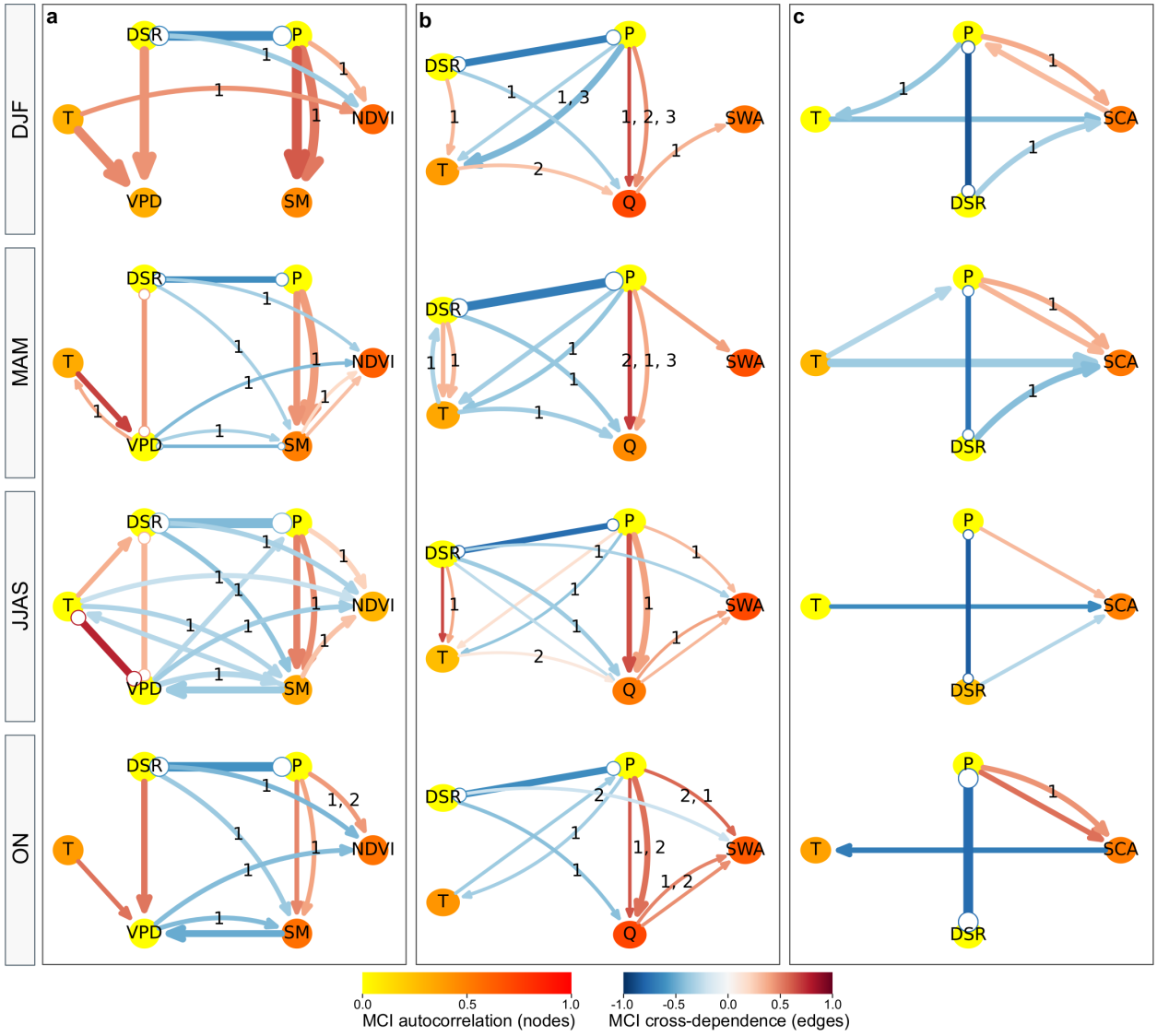

Figure 6: Causal graphs visualizing the relation between the environmental time series, including (a) NDVI, (b) SWA, and (c) SCA. The graphs are calculated for each subbasin and then aggregated for the entire study area at seasonal scale. We used a maximum temporal lag of 3 time steps. Thin edges express low occurrence of the link at basin scale and vice versa. Straight edges denote contemporaneous and curved edges lagged links. The temporal lag is indicated by the number on the curved edges. Links where the direction could not be resolved are indicated by circle ends. Following variables are considered: precipitation (P), soil moisture (SM), temperature (T), surface solar radiation downward (DSR), vapor pressure deficit (VPD), river discharge (Q), NDVI, SWA, and SCA.

4. Discussion

In this study, we quantified land surface dynamics by means of multivariate time series for the large river basins Indus, Ganges, Brahmaputra, and Meghna in South Asia. The results revealed significant

Table 2: Annual and seasonal trends for NDVI stratified by land cover data for the period between 2003 and 2020. All trend values are computed at decadal scale. Bold values represent statistically significant trends (p-value < 0.05). GB: Ganges river basin. BB: Brahmaputra. MB: Meghna. IB: Indus. GBMD: GBM-Delta.

Basin	Class	DJF	MAM	JJAS	ON	Annual
Ganges	Cropland	**0.060**	**0.033**	**0.033**	0.008	**0.033**
	Irrigation	**0.062**	**0.041**	**0.036**	0.004	**0.038**
	Forest	**0.022**	**0.027**	0.009	**0.013**	**0.017**
	Grassland	**0.027**	**0.021**	0.008	**0.019**	**0.020**
Brahmaputra	Cropland	**0.021**	**0.028**	**0.021**	**0.016**	**0.021**
	Irrigation	**0.043**	**0.065**	**0.030**	**0.035**	**0.039**
	Forest	**0.014**	**0.016**	0.002	**0.020**	**0.015**
	Grassland	**0.010**	**0.005**	0.004	**0.015**	**0.008**
Meghna	Cropland	**0.025**	**0.043**	**0.031**	**0.009**	**0.028**
	Irrigation	**0.038**	**0.046**	**0.056**	**0.028**	**0.042**
	Forest	**0.022**	**0.034**	**0.004**	**0.011**	**0.017**
	Grassland	**0.017**	**0.014**	0.001	**0.019**	**0.015**
Indus	Cropland	**0.031**	**0.029**	**0.030**	0.010	**0.029**
	Irrigation	**0.051**	**0.038**	**0.046**	**0.019**	**0.042**
	Forest	**0.025**	**0.036**	**0.017**	0.013	**0.021**
	Grassland	**0.013**	**0.018**	**0.011**	0.006	**0.012**
GBM-Delta	Cropland	**0.019**	**0.036**	**0.039**	**0.011**	**0.028**
	Irrigation	**0.043**	**0.061**	**0.037**	0.026	**0.040**
	Forest	**0.023**	**0.024**	0.006	0.016	**0.019**
	Grassland	**0.016**	**0.097**	**0.045**	**0.008**	**0.031**

positive trends of the NDVI at seasonal temporal scale and spatially at basin as well as grid scale. Previous investigations on vegetation dynamics covering parts of our study area identified comparable greening trends (Chen et al., 2019; Lamchin et al., 2018; Sarmah et al., 2018; Zhou and Ismaeel, 2020). Our results additionally reveal spatial patterns of seasonal trends and trends differentiated by land cover and land use classes at basin scale until the end of 2020. Based on this comprehensive and stratified trend analysis, we demonstrate that irrigated and rainfed croplands significantly contribute to vegetation greening (Table 2). In addition, the relation between trends of remote sensing-based anthropogenic as well as disaggregated census data and NDVI at subbasin scale were quantified. The significant positive correlation supports the assumption that human activities and land use management are an important factor controlling vegetation greening (Mishra and Mainali, 2017). However, the analysis of anthropogenic forcing remains challenging in several ways. For example, time series on socioeconomic data are constrained through administrative boundaries or coarse temporal intervals of the time series. Additional trend analyses reveal that the increase of NDVI is significantly higher during the second part of the studied period compared to the first (Table S3). This finding also applies to the stratified vegetation classes, but particularly to rainfed and irrigated croplands (Table S4, Table S5). Considering climate and hydrological drivers, our results likely reflect that vegetation greenness depends most on water availability. Particularly in the arid and semi-arid regions of the Indus and Ganges plains, soil moisture appears to be the dominant factor throughout the seasons (Fig 5a). In high altitudes, temperature is the limiting climatic factor. Yet, the results suggest that soil moisture is controlling vegetation greenness during monsoon season (Fig 5a). Furthermore, the results suggest that vapor pressure

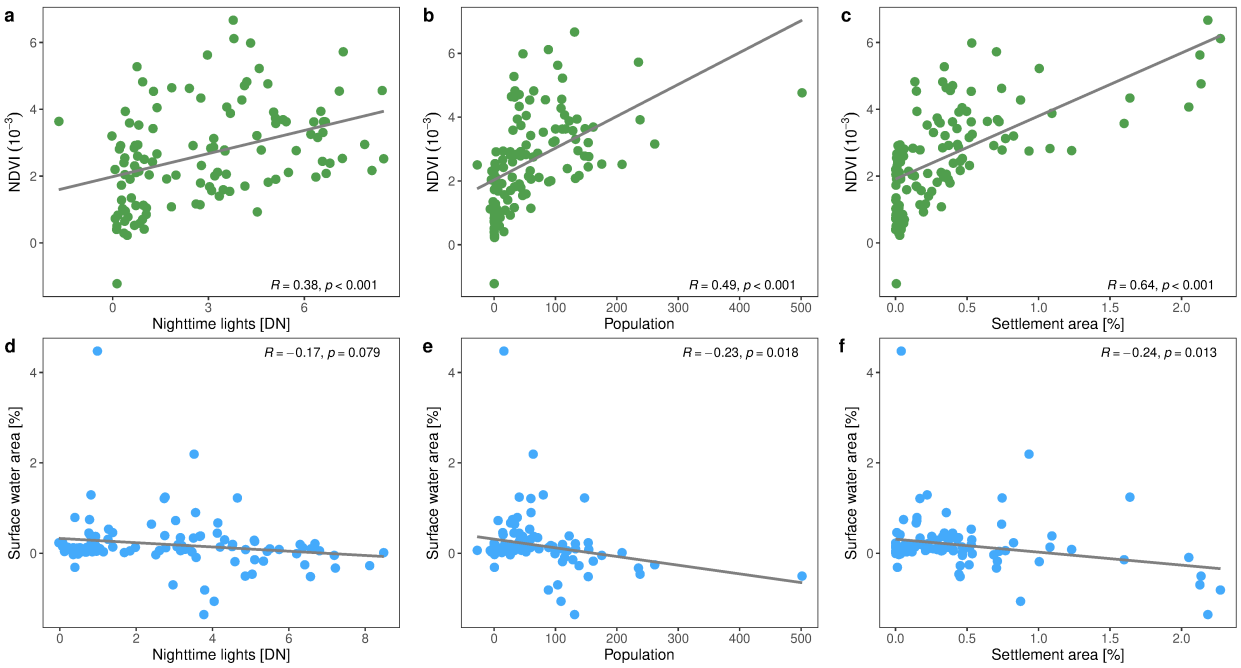

Figure 7: Relation between trends of the land surface variables (a–c) NDVI and (d–f) SWA and anthropogenic factors. The trends are calculated for each subbasin at annual scale. Each dot represents a subbasin.

deficit could be an important factor influencing NDVI negatively during the monsoon season in the upper Indus plain. This finding can be explained by the late onset of monsoon rainfall in the Indus river basin and the influence of the dry pre-monsoon period through temporal lags (Fig. S3). Also, the results show an absence of significant causal links at grid scale in the Indo-Gangetic belt through all seasons, most pronounced in the post-monsoon and winter season (Fig 5a). In this region, groundwater is largely extracted for irrigation purposes (Biemans et al., 2019), thus, it is likely an important controlling factor with respect to vegetation greenness. However, we did not include terrestrial water storage in the causal analysis due to the limited temporal availability and the very coarse spatial resolution of the time series. Considering SWA, we identified a negative impact on vegetation greenness along the large river streams of the Ganges and Brahmaputra as well as the wetlands in the Meghna river basin, especially during the monsoon and post-monsoon season, most likely due to an increase in SWA and flooding (Fig 5a).

With respect to SWA, we found that significant trends are largely positive at grid (Fig. 4b) as well as basin scale (Table 1). At the same time, trend analysis of TWSA reveals significant negative trends for all basins at seasonal as well as annual temporal scale (Table 1, Fig. S1). In this regard, Rodell et al. (2018) explained decreasing terrestrial water storage primarily with groundwater withdrawal for irrigation purposes in the western parts of the river basins and groundwater withdrawal as well as decrease in rainfall for the eastern regions. In addition, Dangar and Mishra (2021) highlight the impacts of long-term changes in climate in the Ganges river basin, which led to higher frequencies of droughts, warming temperature, and a decrease in monsoon rainfall. Zhu et al. (2021) suggest similar reasons for negative trends in TWSA in the Indus

river plains and additionally emphasize the high loss in groundwater during the pre-monsoon and monsoon season. The mismatch between trends in SWA and TWSA might be explained by the contribution of rainfall, glacier as well as snow melt, which might prevent a decrease in SWA. Likewise, groundwater and freshwater withdrawal is at a high level, impeding recharge of terrestrial water storage. Besides irrigation, water supply is additionally pressured by an increasing population, hydropower, and further industrial sectors (Biemans et al., 2019; Viviroli et al., 2020). In this context, our correlation analysis of trends in SWA and anthropogenic factors revealed weak negative relationships, yet being partially significant (Fig. 7d–f). This finding suggests that increases in SWA more likely appear in areas with a reduced increase in population and settlement area.

In the Himalaya-Karakoram region, snow and glacier melt have a pivotal role in modulating water availability in downstream areas, particularly in drought years (Bhattacharya et al., 2021; Miles et al., 2021). Snow cover in this region accumulates between the post-monsoon and winter season reaching its maximum extent around February and March, while the pre-monsoon and monsoon season is characterized by ablation (Fig. S8). We presented seasonal trends of SCA from December 2002 to November 2020 at grid scale, which remained unexplored so far. In detail, partially significant decreasing and increasing trends at seasonal scale were shown (Fig. 4c), whereas trends at basin scale remained mostly insignificant indicating stable SCA (Table 1). The identified significant decreasing trends at grid scale are most pronounced in the Ganges and Brahmaputra river basins during the monsoon and post-monsoon season. At basin scale, the general direction of previously reported trends and insignificant tendencies appear to continue (Ackroyd et al., 2021; Gurung et al., 2017; Wang et al., 2017). In fact, ancillary trend analysis indicates that during the first part of the study period (2002–2012) trends and tendencies in SCA are rather negative at annual scale, whereas the second period (2010–2020) resulted in positive tendencies (Table S3). Furthermore, trend analysis with respect to elevation zones at basin scale reveals a significant decline of SCA between the monsoon and winter season for altitudes greater than 6000 m in the Ganges and Brahmaputra river basins (Fig. S9). During the pre-monsoon season, these trends are significantly positive (Fig. S9). Considering direct influence factors on SCA at seasonal and grid scale, the high influence of precipitation during winter can be explained by westerly disturbances (Cannon et al., 2015; Das and Meher, 2019; Farinotti et al., 2020). The positive influence of precipitation is particularly strong over the Upper Indus and Ganges river basins, while temperature negatively controls SCA and appears to be linked contemporaneously during the monsoon season (Fig. S7). The quantification of indirect links additionally revealed that temperature is negatively impacted by precipitation via SCA in the post-monsoon season (Fig. 6c), which might be explained by the snow-albedo feedback.

Future climate change is expected to control land surface dynamics in the Indo-Gangetic river basins. Temperature increase is particularly amplified in high altitudes (Pepin et al., 2015), leading to a reduction in snow cover and loss of glacier mass (Bhattacharya et al., 2021; Miles et al., 2021). However, as revealed by the trend analyses of SCA, the upper Indus river basin is not yet affected by this decline. This phenomenon is referred to as the Karakoram anomaly (Dimri, 2021). Nevertheless, with accelerating global warming it is

not likely that the anomaly and positive glacier mass budgets will prevail in the long term (Farinotti et al., 2020). In case seasonality and amplitude of snow cover and glacier mass change, large social and economic impacts can be expected, as the downstream population and food production in the Indo-Gangetic Plain depend on meltwater from the mountains, particularly in the Indus and Ganges river basins (Biemans et al., 2019; Pritchard, 2019; Kraaijenbrink et al., 2021; Viviroli et al., 2020). Specifically, during the last two decades, the peak in SCA is reached between February and March (Fig. S8). Thus, any changes in SCA and the ablation period will likely modulate the runoff and possibly shift the peak in river discharge and SWA (Fig. S10) having consequences, i.e. on irrigation and cropping systems. On the other hand, land use change and intensive irrigation influence the regional climate (Mishra et al., 2020; Singh et al., 2018), which in turn appears to affect precipitation and hence, glacier formation in high altitudes (de Kok et al., 2018). In the light of declining terrestrial water storage and a projected increase of droughts and heatwaves, it remains questionable how long the agricultural intensification will sustain in the investigated river basins.

5. Conclusion

This study is the first to investigate multivariate time series, including climatic, hydrological and multiple remote sensing-based land surface variables with biweekly temporal resolution at seasonal and annual scale. We investigated the period December 2002 to November 2020 across the large river basins Indus, Ganges, Brahmaputra, and Meghna in South Asia. These time series were used to perform statistical trend analysis at grid and basin scale revealing following findings:

- Increasing trends in vegetation greenness were particularly pronounced over irrigated and rainfed croplands, e.g., in the Indus river basin the trends at annual scale amount to 0.042 and 0.029 NDVI/decade^{-1}, respectively. Moreover, vegetation trends accelerated during the second part of the study period, compared to the first. For example at annual scale, vegetation greenness increases by 0.019 during the first and by 0.037 NDVI/decade^{-1} during the second part in the Ganges river basin.
- Regarding surface water area, the trends point towards positive values in the Indus (0.074 %/decade^{-1}) and Ganges (0.071 %/decade^{-1}) river basins as well as in the GBM-Delta (0.407 %/decade^{-1}) at basin and annual temporal scale. At grid and seasonal temporal scale, we detected clusters with significant negative trends over the Meghna river basin and the GBM-Delta. The share of significant negative trends was highest during the winter (11.1 %) and post-monsoon (7.7 %) season.
- At basin scale, trends in snow cover area were insignificant throughout all seasons and at annual scale, except for the monsoon season in the Ganges (–0.218 %/decade^{-1}) and for the post-monsoon season in the Brahmaputra (–1.350 %/decade^{-1}) river basin. Likewise, negative trends were identified for the Upper Ganges and Brahmaputra river basins being distinct during the monsoon and post-monsoon season at grid scale. The percentage of negative trends amounts to 10.2 % and 14.3 %, respectively.

To analyze direct and indirect controls on land surface variables, causal networks were computed. At grid scale, we found that NDVI is mostly controlled by water availability through the soil and atmosphere. Considering surface water area, a positive coupling with river discharge exists in the downstream areas. In the Upper basins, snow cover area and temperature are negatively linked to surface water area. Regarding snow cover area, temperature and precipitation are the dominant driving variables with spatial variations over the seasons. During the monsoon season, temperature is negatively coupled to snow cover area, whereas precipitation has high positive influence particularly during the winter. At basin scale, the evaluation of indirect links deciphers known mechanisms such as the cooling of air temperature through soil moisture and precipitation as well as the snow-albedo feedback. Here, the causal graphs highlight the potential of detecting indirect links which are not visible at grid scale. The investigation of the relation between vegetation greenness and anthropogenic factors implied significant positive correlation likely reflecting the impact, i.e. of land use management.

With ongoing climate and environmental change, future research with longer time series on remote sensing-based land surface variables will deepen the understanding of the complex interplays with climatic, hydrological, and anthropogenic controls. Our findings are important for the interpretation of trends and drivers of land surface variables in the Indus, Ganges, Brahmaputra, and Meghna river basins. In addition, the methodological approach of this study allows exploration of the interactions between multiple spheres providing valuable insight into the analysis of land surface dynamics and driving factors over any other large river basin.

Data availability statement

The HydroSHED data was downloaded from `https://www.hydrosheds.org/downloads`. We obtained the ESA CCI Land Cover data at `http://www.esa-landcover-cci.org/`. The Copernicus DEM is available after registration at `https://spacedata.copernicus.eu/explore-more/news-archive/-/asset_publisher/Ye8egYeRPLEs/blog/id/434960`. We downloaded MODIS Surface Reflectance data from `https://lpdaac.usgs.gov/products/mod09gav006/`. The DLR Global SnowPack, the DLR Global WaterPack, and DLR World Settlement Footprint are available upon request. The harmonized nighttime lights dataset was downloaded from `https://doi.org/10.6084/m9.figshare.9828827.v2`. The gridded population data can be retrieved at `https://www.worldpop.org/geodata/`. The climatic (ERA5-Land) and hydrological variables (GloFAS-ERA5) are available at `https://cds.climate.copernicus.eu/`.

References

Ackroyd, C., Skiles, S.M., Rittger, K., Meyer, J., 2021. Trends in Snow Cover Duration Across River Basins in High Mountain Asia From Daily Gap-Filled MODIS Fractional Snow Covered Area. Front. Earth Sci. 9, 713145. doi:10.3389/feart.2021.713145.

Airbus, 2020. Copernicus DEM Product Handbook. URL: spacedata.copernicus.eu/documents/20126/0/GEO1988-CopernicusDEM-SPE-002_ProductHandbook_I3.0.pdf.

Azam, M.F., Kargel, J.S., Shea, J.M., Nepal, S., Haritashya, U.K., Srivastava, S., Maussion, F., Qazi, N., Chevallier, P., Dimri, A.P., Kulkarni, A.V., Cogley, J.G., Bahuguna, I.M., 2021. Glaciohydrology of the Himalaya-Karakoram. Science 373, eabf3668. doi:10.1126/science.abf3668.

Barkhordarian, A., Saatchi, S.S., Behrangi, A., Loikith, P.C., Mechoso, C.R., 2019. A Recent Systematic Increase in Vapor Pressure Deficit over Tropical South America. Sci. Rep. 9, 15331. doi:10.1038/s41598-019-51857-8.

Beck, H.E., Zimmermann, N.E., McVicar, T.R., Vergopolan, N., Berg, A., Wood, E.F., 2018. Present and future Koppen-Geiger climate classification maps at 1-km resolution. Sci. Data 5, 180214. doi:10.1038/sdata.2018.214.

Bhattacharya, A., Bolch, T., Mukherjee, K., King, O., Menounos, B., Kapitsa, V., Neckel, N., Yang, W., Yao, T., 2021. High Mountain Asian glacier response to climate revealed by multi-temporal satellite observations since the 1960s. Nat. Commun. 12, 4133. doi:10.1038/s41467-021-24180-y.

Biemans, H., Siderius, C., Lutz, A.F., Nepal, S., Ahmad, B., Hassan, T., von Bloh, W., Wijngaard, R.R., Wester, P., Shrestha, A.B., Immerzeel, W.W., 2019. Importance of snow and glacier meltwater for agriculture on the Indo-Gangetic Plain. Nat. Sustain. 2, 594–601. doi:10.1038/s41893-019-0305-3.

Cannon, F., Carvalho, L.M.V., Jones, C., Norris, J., 2015. Winter westerly disturbance dynamics and precipitation in the western Himalaya and Karakoram: a wave-tracking approach. Theor. Appl. Climatol. 125, 27–44. doi:10.1007/s00704-015-1489-8.

Chen, C., Park, T., Wang, X., Piao, S., Xu, B., Chaturvedi, R.K., Fuchs, R., Brovkin, V., Ciais, P., Fensholt, R., Tommervik, H., Bala, G., Zhu, Z., Nemani, R.R., Myneni, R.B., 2019. China and India lead in greening of the world through land-use management. Nat. Sustain. 2, 122–129. doi:10.1038/s41893-019-0220-7.

Collaud Coen, M., Andrews, E., Bigi, A., Martucci, G., Romanens, G., Vogt, F.P.A., Vuilleumier, L., 2020. Effects of the prewhitening method, the time granularity, and the time segmentation on the Mann–Kendall trend detection and the associated Sen's slope. Atmos. Meas. Tech. 13, 6945–6964. doi:10.5194/amt-13-6945-2020.

Dangar, S., Mishra, V., 2021. Natural and anthropogenic drivers of the lost groundwater from the Ganga River basin. Environ. Res. Lett. 16, 114009. doi:10.1088/1748-9326/ac2ceb.

Das, L., Meher, J.K., 2019. Drivers of climate over the Western Himalayan region of India: A review. Earth-Sci. Rev. 198, 102935. doi:10.1016/j.earscirev.2019.102935.

Di Capua, G., Runge, J., Donner, R.V., van den Hurk, B., Turner, A.G., Vellore, R., Krishnan, R., Coumou, D., 2020. Dominant patterns of interaction between the tropics and mid-latitudes in boreal summer: causal relationships and the role of timescales. Weather Clim. Dyn. 1, 519–539. doi:10.5194/wcd-1-519-2020.

Dietz, A.J., Kuenzer, C., Dech, S., 2015. Global SnowPack: a new set of snow cover parameters for studying status and dynamics of the planetary snow cover extent. Remote Sens. Lett. 6, 844–853. doi:10.1080/2150704X.2015.1084551.

Dimri, A.P., 2021. Decoding the Karakoram Anomaly. Sci. Total Environ. 788, 147864. doi:10.1016/j.scitotenv.2021.147864.

European Space Agency, Sinergise, 2021. Copernicus Global Digital Elevation Model. Distributed by OpenTopography. doi:10.5069/G9028PQB. (Last accessed on: 2022-02-01).

Farinotti, D., Immerzeel, W.W., de Kok, R., Quincey, D.J., Dehecq, A., 2020. Manifestations and mechanisms of the Karakoram glacier Anomaly. Nat. Geosci. 13, 8–16. doi:10.1038/s41561-019-0513-5.

Gorelick, N., Hancher, M., Dixon, M., Ilyushchenko, S., Thau, D., Moore, R., 2017. Google Earth Engine: Planetary-scale geospatial analysis for everyone. Remote Sens. Environ. 202, 18–27. doi:10.1016/j.rse.2017.06.031.

Gurung, D.R., Maharjan, S.B., Shrestha, A.B., Shrestha, M.S., Bajracharya, S.R., Murthy, M.S.R., 2017. Climate and topographic controls on snow cover dynamics in the Hindu Kush Himalaya. Int. J. Climatol. 37, 3873–3882. doi:10.1002/joc.4961.

Harrigan, S., Zsoter, E., Alfieri, L., Prudhomme, C., Salamon, P., Wetterhall, F., Barnard, C., Cloke, H., Pappenberger, F., 2020. GloFAS-ERA5 operational global river discharge reanalysis 1979–present. Earth Syst. Sci. Data 12, 2043–2060. doi:10.5194/essd-12-2043-2020.

Hasson, S., Böhner, J., Lucarini, V., 2017. Prevailing climatic trends and runoff response from Hindukush–Karakoram–Himalaya, upper Indus Basin. Earth Syst. Dyn. 8, 337–355. doi:10.5194/esd-8-337-2017.

Janes, T., McGrath, F., Macadam, I., Jones, R., 2019. High-resolution climate projections for South Asia to inform climate impacts and adaptation studies in the Ganges-Brahmaputra-Meghna and Mahanadi deltas. Sci. Total Environ. 650, 1499–1520. doi:10.1016/j.scitotenv.2018.08.376.

Klein, I., Gessner, U., Dietz, A.J., Kuenzer, C., 2017. Global WaterPack – A 250m resolution dataset revealing the daily dynamics of global inland water bodies. Remote Sens. Environ. 198, 345–362. doi:10.1016/j.rse.2017.06.045.

Klein, I., Mayr, S., Gessner, U., Hirner, A., Kuenzer, C., 2021. Water and hydropower reservoirs: High temporal resolution time series derived from MODIS data to characterize seasonality and variability. Remote Sens. Environ. 253, 112207. doi:10.1016/j.rse.2020.112207.

de Kok, R.J., Tuinenburg, O.A., Bonekamp, P.N.J., Immerzeel, W.W., 2018. Irrigation as a Potential Driver for Anomalous Glacier Behavior in High Mountain Asia. Geophys. Res. Lett. 45, 2047–2054. doi:10.1002/2017GL076158.

Kolluru, V., Kolluru, S., Konkathi, P., 2020. Evaluation and integration of reanalysis rainfall products under contrasting climatic conditions in India. Atmos. Res. 246, 105121. doi:10.1016/j.atmosres.2020.105121.

Kraaijenbrink, P.D.A., Stigter, E.E., Yao, T., Immerzeel, W.W., 2021. Climate change decisive for Asia's snow meltwater supply. Nat. Clim. Chang. 11, 591–597. doi:10.1038/s41558-021-01074-x.

Kvas, A., Behzadpour, S., Ellmer, M., Klinger, B., Strasser, S., Zehentner, N., Mayer-Gürr, T., 2019. ITSG-Grace2018: Overview and Evaluation of a New GRACE-Only Gravity Field Time Series. J. Geophys. Res. Solid Earth 124, 9332–9344. doi:10.1029/2019jb017415.

Lamchin, M., Lee, W.K., Jeon, S.W., Wang, S.W., Lim, C.H., Song, C., Sung, M., 2018. Long-term trend and correlation between vegetation greenness and climate variables in Asia based on satellite data. Sci. Total Environ. 618, 1089–1095. doi:10.1016/j.scitotenv.2017.09.145.

Lehner, B., Verdin, K., Jarvis, A., 2008. New global hydrography derived from spaceborne elevation data. Eos, Transactions American Geophysical Union 89, 93–94.

Li, M., Wu, P., Ma, Z., 2020. A comprehensive evaluation of soil moisture and soil temperature from third-generation atmospheric and land reanalysis data sets. Int. J. Climatol. 40, 5744–5766. doi:10.1002/joc.6549.

Li, X., Zhou, Y., 2017. A Stepwise Calibration of Global DMSP/OLS Stable Nighttime Light Data (1992–2013). Remote Sens. 9, 637. doi:10.3390/rs9060637.

Liu, Y., Li, Z., Chen, Y., 2021. Continuous warming shift greening towards browning in the Southeast and Northwest High Mountain Asia. Sci. Rep. 11, 17920. doi:10.1038/s41598-021-97240-4.

Lloyd, C.T., Chamberlain, H., Kerr, D., Yetman, G., Pistolesi, L., Stevens, F.R., Gaughan, A.E., Nieves, J.J., Hornby, G., MacManus, K., Sinha, P., Bondarenko, M., Sorichetta, A., Tatem, A.J., 2019. Global spatio-temporally harmonised datasets for producing high-resolution gridded population distribution datasets. Big Earth Data 3, 108–139. doi:10.1080/20964471.2019.1625151.

MacDonald, A.M., Bonsor, H.C., Ahmed, K.M., Burgess, W.G., Basharat, M., Calow, R.C., Dixit, A., Foster, S.S.D., Gopal, K., Lapworth, D.J., Lark, R.M., Moench, M., Mukherjee, A., Rao, M.S., Shamsudduha, M., Smith, L., Taylor, R.G., Tucker, J., van Steenbergen, F., Yadav, S.K., 2016. Groundwater quality and depletion in the Indo-Gangetic Basin mapped from in situ observations. Nat. Geosci. 9, 762–766. doi:10.1038/ngeo2791.

Mahecha, M.D., Gans, F., Brandt, G., Christiansen, R., Cornell, S.E., Fomferra, N., Kraemer, G., Peters, J., Bodesheim, P., Camps-Valls, G., Donges, J.F., Dorigo, W., Estupinan-Suarez, L.M., Gutierrez-Velez, V.H., Gutwin, M., Jung, M., Londoño, M.C., Miralles, D.G., Papastefanou, P., Reichstein, M., 2020. Earth system data cubes unravel global multivariate dynamics. Earth Syst. Dyn. 11, 201–234. doi:10.5194/esd-11-201-2020.

Marconcini, M., Metz-Marconcini, A., Esch, T., Gorelick, N., 2021. Understanding Current Trends in Global Urbanisation - The World Settlement Footprint Suite. GI_Forum 1, 33–38. doi:10.1553/giscience2021_01_s33.

Marconcini, M., Metz-Marconcini, A., Ureyen, S., Palacios-Lopez, D., Hanke, W., Bachofer, F., Zeidler, J., Esch, T., Gorelick, N., Kakarla, A., Paganini, M., Strano, E., 2020. Outlining where humans live, the World Settlement Footprint 2015. Sci. Data 7, 242. doi:10.1038/s41597-020-00580-5.

Mayer-Gürr, T., Behzadpur, S., Ellmer, M., Kvas, A., Klinger, B., Strasser, S., Zehentner, N., 2018. ITSG-Grace2018–Monthly, Daily and Static Gravity Field Solutions from GRACE, GFZ Data Services. doi:10.5880/ICGEM.2018.003.

Miles, E., McCarthy, M., Dehecq, A., Kneib, M., Fugger, S., Pellicciotti, F., 2021. Health and sustainability of glaciers in High Mountain Asia. Nat. Commun. 12, 2868. doi:10.1038/s41467-021-23073-4.

Mishra, N.B., Mainali, K.P., 2017. Greening and browning of the Himalaya: Spatial patterns and the role of climatic change and human drivers. Sci. Total Environ. 587-588, 326–339. doi:10.1016/j.scitotenv.2017.02.156.

Mishra, V., Ambika, A.K., Asoka, A., Aadhar, S., Buzan, J., Kumar, R., Huber, M., 2020. Moist heat stress extremes in India enhanced by irrigation. Nat. Geosci. 13, 722–728. doi:10.1038/s41561-020-00650-8.

Mondal, S.K., Tao, H., Huang, J., Wang, Y., Su, B., Zhai, J., Jing, C., Wen, S., Jiang, S., Chen, Z., Jiang, T., 2021. Projected changes in temperature, precipitation and potential evapotranspiration across Indus River Basin at 1.5-3.0 degrees C warming levels using CMIP6-GCMs. Sci. Total Environ. 789, 147867. doi:10.1016/j.scitotenv.2021.147867.

Muñoz-Sabater, J., 2019. ERA5-Land hourly data from 1981 to present. Copernicus Climate Change Service (C3S) Climate Data Store (CDS). doi:10.24381/cds.e2161bac. accessed on 01 June 2021.

Nepal, S., Khatiwada, K.R., Pradhananga, S., Kralisch, S., Samyn, D., Bromand, M.T., Jamal, N., Dildar, M., Durrani, F., Rassouly, F., Azizi, F., Salehi, W., Malikzooi, R., Krause, P., Koirala, S., Chevallier, P., 2021. Future snow projections in a small basin of the Western Himalaya. Sci. Total Environ. 795, 148587. doi:10.1016/j.scitotenv.2021.148587.

Nie, Y., Pritchard, H.D., Liu, Q., Hennig, T., Wang, W., Wang, X., Liu, S., Nepal, S., Samyn, D., Hewitt, K., Chen, X., 2021. Glacial change and hydrological implications in the Himalaya and Karakoram. Nat. Rev. Earth Environ. 2, 91–106. doi:10.1038/s43017-020-00124-w.

Notarnicola, C., 2020. Hotspots of snow cover changes in global mountain regions over 2000–2018. Remote Sens. Environ. 243, 111781. doi:10.1016/j.rse.2020.111781.

Pekel, J.F., Cottam, A., Gorelick, N., Belward, A.S., 2016. High-resolution mapping of global surface water and its long-term changes. Nature 540, 418. doi:10.1038/nature20584.

Pepin, N., Bradley, R.S., Diaz, H.F., Baraer, M., Caceres, E.B., Forsythe, N., Fowler, H., Greenwood, G., Hashmi, M.Z., Liu, X.D., Miller, J.R., Ning, L., Ohmura, A., Palazzi, E., Rangwala, I., Schöner, W., Severskiy, I., Shahgedanova, M., Wang, M.B., Williamson, S.N., Yang, D.Q., 2015. Elevation-dependent warming in mountain regions of the world. Nat. Clim. Chang. 5, 424–430. doi:10.1038/nclimate2563.

Pritchard, H.D., 2019. Asia's shrinking glaciers protect large populations from drought stress. Nature 569, 649–654. doi:10.1038/s41586-019-1240-1.

Rößler, S., Witt, M.S., Ikonen, J., Brown, I.A., Dietz, A.J., 2021. Remote Sensing of Snow Cover Variability and Its Influence on the Runoff of Sápmi's Rivers. Geosciences 11, 130. doi:10.3390/geosciences11030130.

Rodell, M., Famiglietti, J.S., Wiese, D.N., Reager, J.T., Beaudoing, H.K., Landerer, F.W., Lo, M.H., 2018. Emerging trends in global freshwater availability. Nature 557, 651–659. doi:10.1038/s41586-018-0123-1.

Runge, J., 2020. Discovering contemporaneous and lagged causal relations in autocorrelated nonlinear time series datasets. URL: http://proceedings.mlr.press/v124/runge20a.html.

Runge, J., Nowack, P., Kretschmer, M., Flaxman, S., Sejdinovic, D., 2019. Detecting and quantifying causal associations in large nonlinear time series datasets. Sci. Adv. 5, eaau4996. doi:10.1126/sciadv.aau4996.

Sarmah, S., Jia, G., Zhang, A., 2018. Satellite view of seasonal greenness trends and controls in South Asia. Environ. Res. Lett. 13, 034026. doi:10.1088/1748-9326/aaa866.

Singh, D., McDermid, S.P., Cook, B.I., Puma, M.J., Nazarenko, L., Kelley, M., 2018. Distinct Influences of Land Cover and Land Management on Seasonal Climate. J. Geophys. Res. Atmos. 123, 12017–12039. doi:10.1029/2018JD028874.

Song, X.P., Hansen, M.C., Stehman, S.V., Potapov, P.V., Tyukavina, A., Vermote, E.F., Townshend, J.R., 2018. Global land change from 1982 to 2016. Nature 560, 639–643. doi:10.1038/s41586-018-0411-9.

Uereyen, S., Kuenzer, C., 2019. A Review of Earth Observation-Based Analyses for Major River Basins. Remote Sens. 11, 2951. doi:10.3390/rs11242951.

Urraca, R., Huld, T., Gracia-Amillo, A., Martinez-de Pison, F.J., Kaspar, F., Sanz-Garcia, A., 2018. Evaluation of global horizontal irradiance estimates from ERA5 and COSMO-REA6 reanalyses using ground and satellite-based data. Sol. Energy 164, 339–354. doi:10.1016/j.solener.2018.02.059.

Viviroli, D., Kummu, M., Meybeck, M., Kallio, M., Wada, Y., 2020. Increasing dependence of lowland populations on mountain water resources. Nat. Sustain. 3, 917–928. doi:10.1038/s41893-020-0559-9.

Wang, W., Chen, Y., Becker, S., Liu, B., 2015. Variance Correction Prewhitening Method for Trend Detection in Autocorrelated Data. J. Hydrol. Eng. 20, 04015033. doi:10.1061/(ASCE)HE.1943-5584.0001234.

Wang, X., Wu, C., Wang, H., Gonsamo, A., Liu, Z., 2017. No evidence of widespread decline of snow cover on the Tibetan Plateau over 2000-2015. Sci. Rep. 7, 14645. doi:10.1038/s41598-017-15208-9.

Wang, X.L., Swail, V.R., 2001. Changes of Extreme Wave Heights in Northern Hemisphere Oceans and Related Atmospheric Circulation Regimes. J. Clim. 14, 2204–2221. doi:10.1175/1520-0442(2001)014<2204:Coewhi>2.0.Co;2.

Wijngaard, R.R., Biemans, H., Lutz, A.F., Shrestha, A.B., Wester, P., Immerzeel, W.W., 2018. Climate change vs. socio-economic development: understanding the future South Asian water gap. Hydrol. Earth Syst. Sci. 22, 6297–6321. doi:10.5194/hess-22-6297-2018.

Wittich, K.P., Hansing, O., 1995. Area-averaged vegetative cover fraction estimated from satellite data. Int. J. Biometeorol. 38, 209–215. doi:10.1007/BF01245391.

Woodcock, C.E., Loveland, T.R., Herold, M., Bauer, M.E., 2020. Transitioning from change detection to monitoring with remote sensing: A paradigm shift. Remote Sens. Environ. 238, 111558. doi:10.1016/j.rse.2019.111558.

Wu, D., Zhao, X., Liang, S., Zhou, T., Huang, K., Tang, B., Zhao, W., 2015. Time-lag effects of global vegetation responses to climate change. Glob. Chang. Biol. 21, 3520–31. doi:10.1111/gcb.12945.

Yang, D., Bright, J.M., 2020. Worldwide validation of 8 satellite-derived and reanalysis solar radiation products: A preliminary evaluation and overall metrics for hourly data over 27 years. Sol. Energy 210, 3–19. doi:10.1016/j.solener.2020.04.016.

Zheng, K., Wei, J.Z., Pei, J.Y., Cheng, H., Zhang, X.L., Huang, F.Q., Li, F.M., Ye, J.S., 2019. Impacts of climate change and human activities on grassland vegetation variation in the Chinese Loess Plateau. Sci. Total Environ. 660, 236–244. doi:10.1016/j.scitotenv.2019.01.022.

Zhou, Q., Ismaeel, A., 2020. Seasonal Cropland Trends and Their Nexus with Agrometeorological Parameters in the Indus River Plain. Remote Sens. 13. doi:10.3390/rs13010041.

Zhu, Y., Liu, S., Yi, Y., Xie, F., Grunwald, R., Miao, W., Wu, K., Qi, M., Gao, Y., Singh, D., 2021. Overview of terrestrial water storage changes over the Indus River Basin based on GRACE/GRACE-FO solutions. Sci. Total Environ. 799, 149366. doi:10.1016/j.scitotenv.2021.149366.

Supplementary material for:

"Seasonal trends and drivers of land surface variables in Indo-Gangetic river basins"

by Soner Uereyen[a], Felix Bachofer[a], Igor Klein[a], Claudia Kuenzer[a,b]

[a] German Remote Sensing Data Center (DFD), German Aerospace Center (DLR), Wessling, Germany

[b] Department of Remote Sensing, Institute of Geography and Geology, University Wuerzburg, Wuerzburg, Germany

Table S1. List of investigated river basins including area and population count extracted from the gridded WorldPop dataset (Lloyd et al. 2019).

Basin	Area [km^2]	Population count
Ganges	954,206	586,119,928
Brahmaputra	540,783	83,723,373
Meghna	95,711	91,212,172
Indus	1,131,090	300,364,670
GBM–Delta	83,568	94,637,377
All basins	2,805,358	1,156,057,520

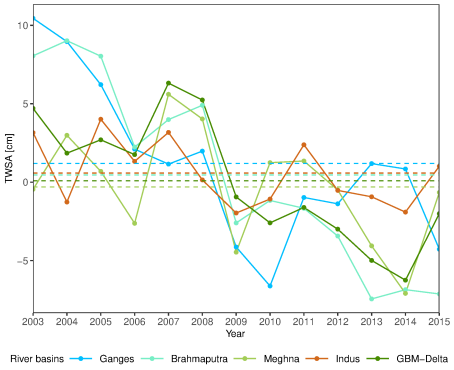

Fig. S1. Terrestrial water storage anomaly at annual scale.

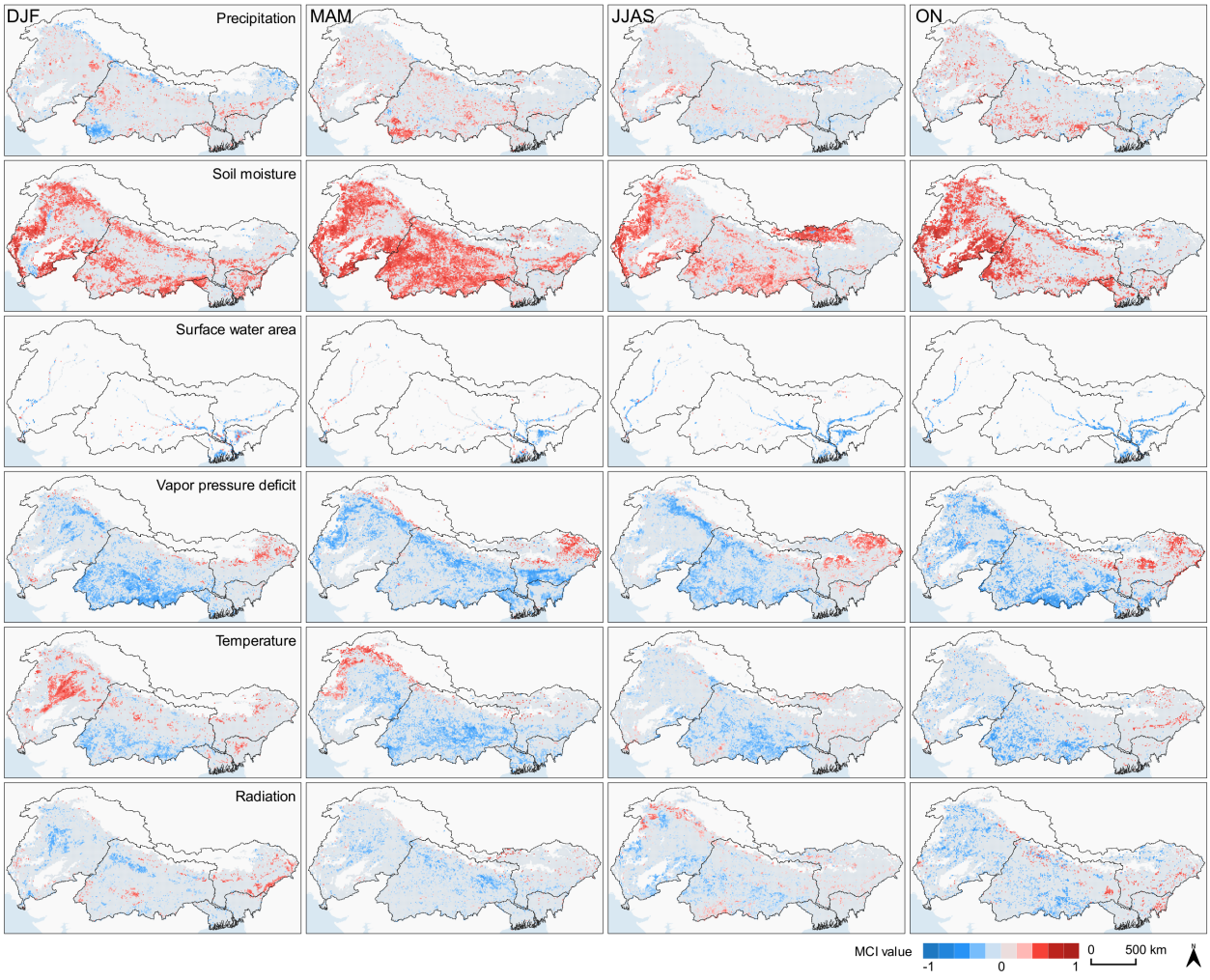

Fig. S2. Target variable: Normalized difference vegetation index. PCMCI$^+$ is used to compute influence of driving variables on the target variable at seasonal scale. Highest absolute MCI value is displayed per grid.

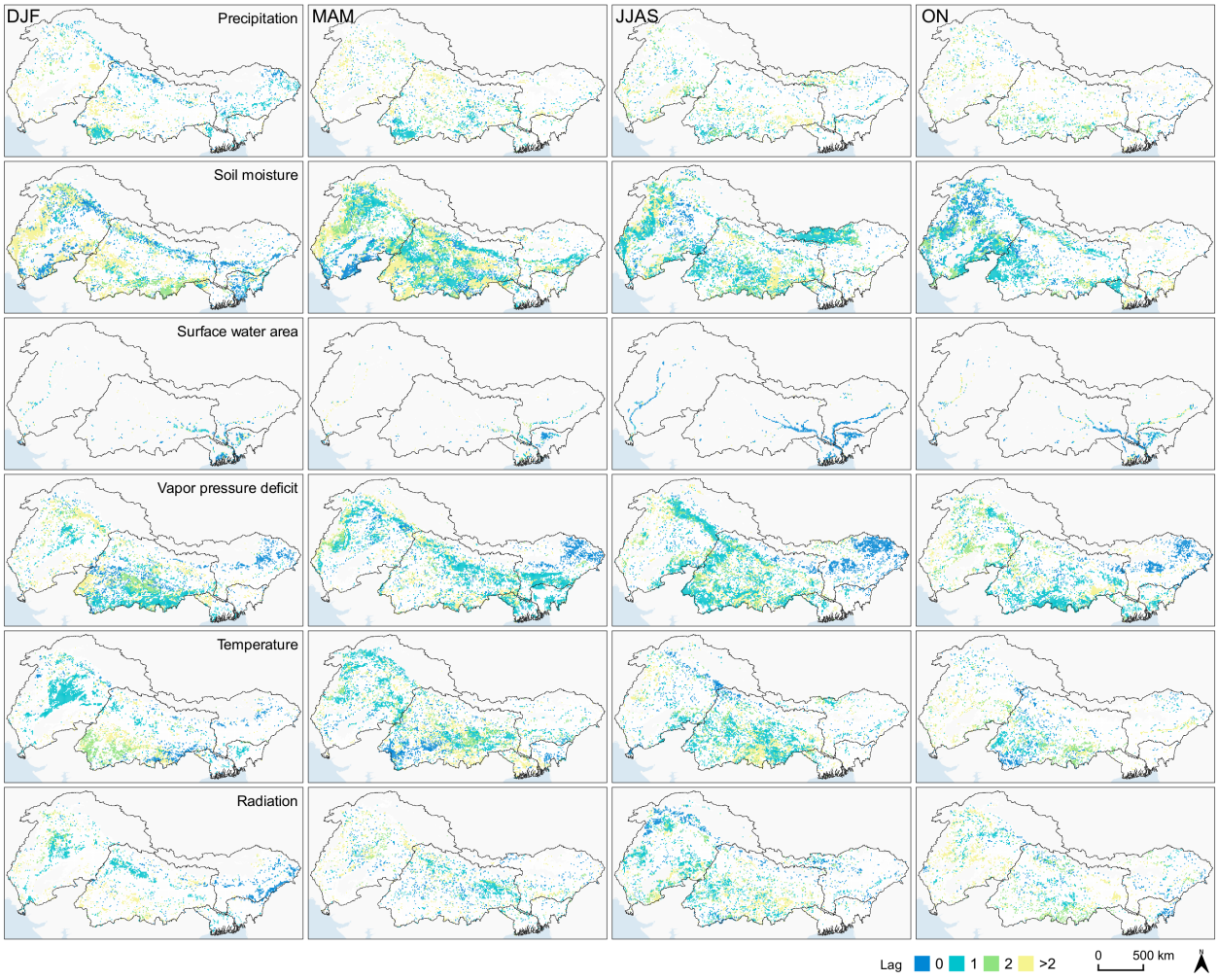

Fig. S3. Target variable: Normalized difference vegetation index. Temporal lags (biweekly) with highest absolute MCI value are displayed for the driving variables.

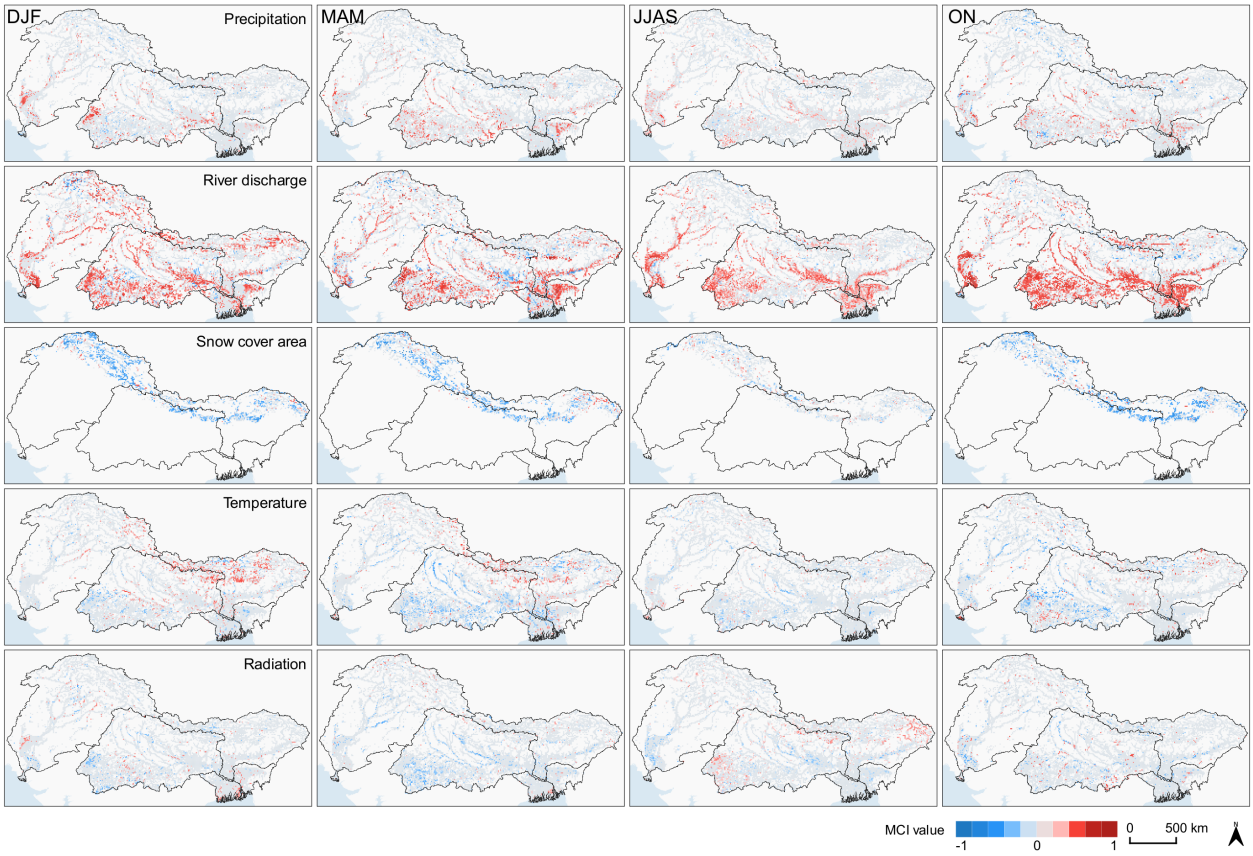

Fig. S4. Target variable: Surface water area. PCMCI$^+$ is used to compute influence of driving variables on the target variable at seasonal scale. Highest absolute MCI value is displayed per grid.

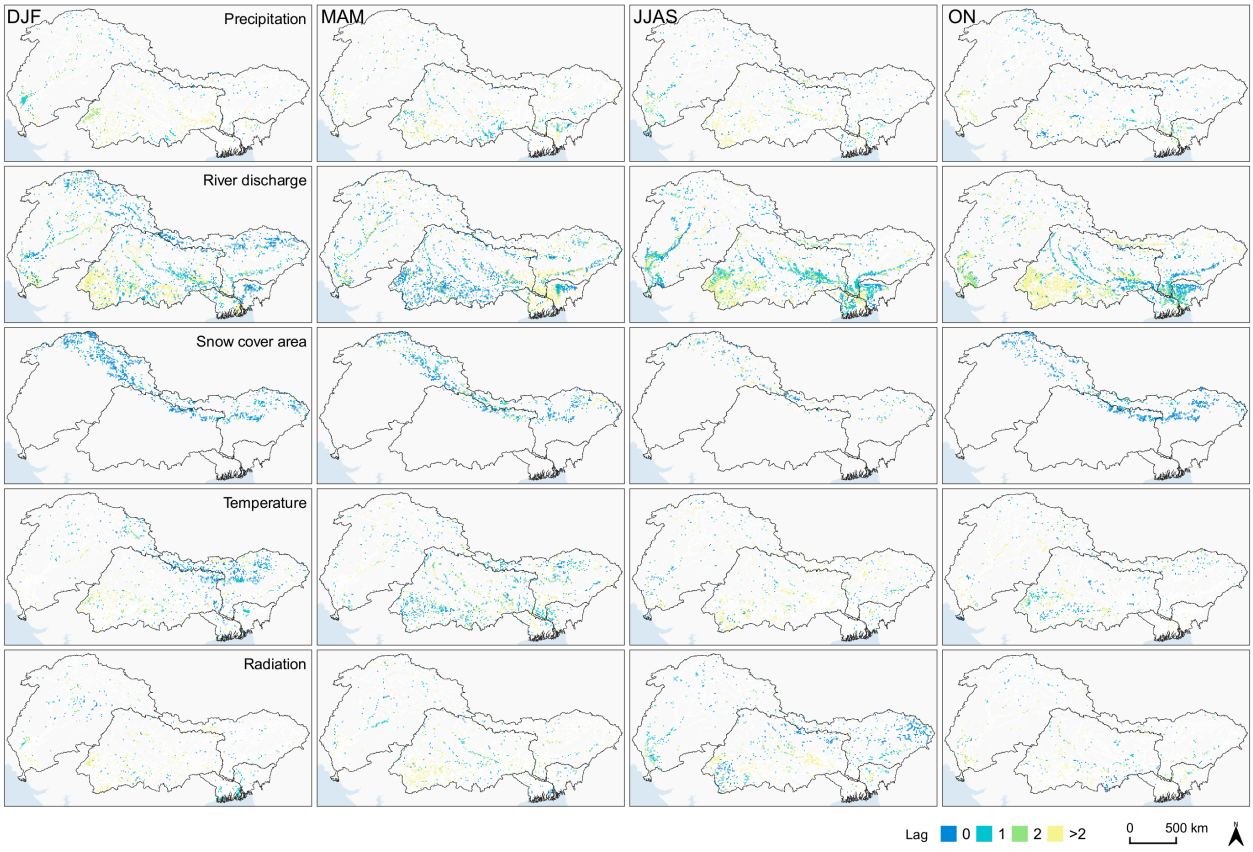

Fig. S5. Target variable: Surface water area. Temporal lags (biweekly) with highest absolute MCI value are displayed for the driving variables.

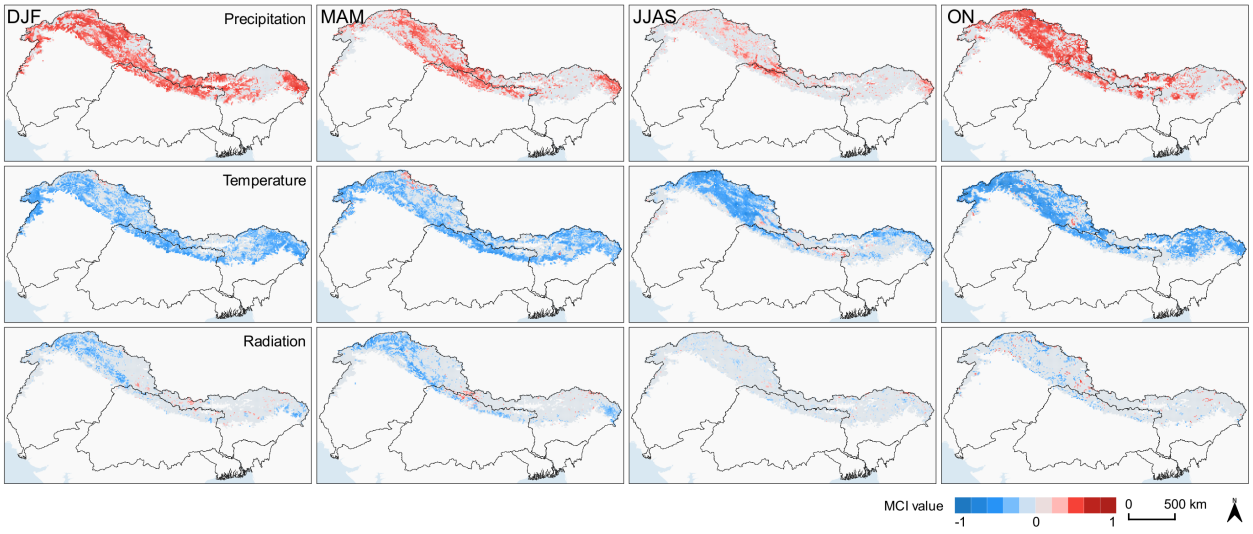

Fig. S6. Target variable: Snow cover area. PCMCI$^+$ is used to compute influence of driving variables on the target variable at seasonal scale. Highest absolute MCI value is displayed per grid.

Table S2. Summary of selected settings for PCMCI$^+$ framework. For further details the reader is referred to Runge et al. (2019) and Runge (2020).

Parameter	**Description**	**Used value**
Dataframe	Includes time series variables and temporal information. If data mask is used, it is appended to the dataframe.	Targets & drivers
Data mask	Mask defining time steps to include and exclude (0: False, 1: True).	Meteorological seasons
Mask type	Definition of which variables and time steps to mask. E.g. type "y" masks target variable as defined in mask, but allows drivers depending on temporal lags to be outside of mask.	"y"
Lags	Temporal lags to test (minimum, maximum).	min:0, max:6
Independence test	Conditional independence test including linear (e.g. partial correlation) and nonlinear dependencies.	"ParCorr"
α_{pc}	Significance threshold in condition selection step (PC1), comparable to hyperparameter optimization in model selection process. If "None" is used, optimal value is selected via Akaike information criterion score.	"None"
α	Threshold to extract significant links detected for each target variable in MCI test.	0.05
Selected links	Definition of potential causal links to be tested. A detailed specification of a target variable, potential parents, and maximum lags is possible. We only consider parents for the three target variables.	$X^i_{t-\tau} \to X^j_t$
False discovery rate	Parameter to account for inflated p–value due to multiple testing in MCI step.	"fdr_bh"

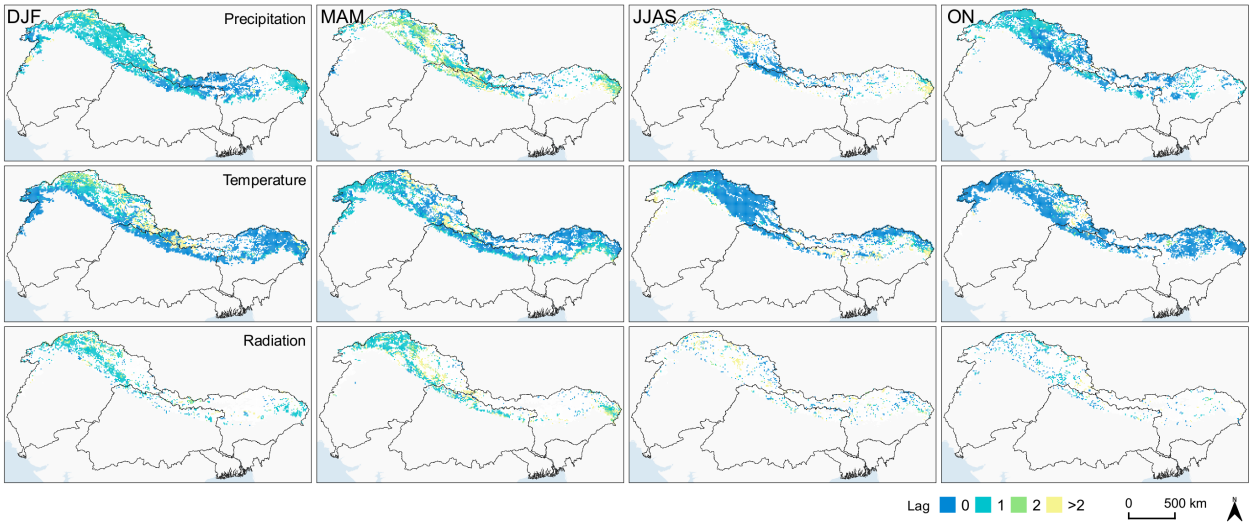

Fig. S7. Target variable: Snow cover area. Temporal lags (biweekly) with highest absolute MCI value are displayed for the driving variables.

Table S3. Annual and seasonal trends at basin scale. All trend values are computed at decadal scale. Bold values represent significant trends (p–value < 0.05).

		2002–2012			2010–2020		
Basin	Season	NDVI	SWA [%]	SCA [%]	NDVI	SWA [%]	SCA [%]
Ganges	DJF	**0.044**	**0.035**	–0.447	**0.050**	0.125	0.285
	MAM	**0.010**	**0.081**	–0.394	**0.041**	0.023	0.511
	JJAS	0.027	–0.022	–0.029	0.033	0.057	–0.392
	ON	0.007	–0.020	**–0.677**	0.004	0.128	0.217
	Annual	**0.019**	0.008	–0.420	**0.037**	0.091	0.251
Brahmaputra	DJF	**–0.022**	0.190	–3.786	**0.040**	–0.031	1.796
	MAM	–0.016	–0.052	–0.729	**0.050**	0.015	2.561
	JJAS	0.007	–0.084	0.441	–0.002	**0.405**	–0.960
	ON	0.016	–0.149	–2.073	0.003	**0.251**	–0.446
	Annual	–0.004	–0.068	**–1.401**	**0.022**	**0.133**	0.675
Meghna	DJF	**–0.019**	1.543	–	**0.075**	–0.309	–
	MAM	–0.002	–0.128	–	**0.082**	0.384	–
	JJAS	**0.037**	**–0.795**	–	0.002	**0.669**	–
	ON	0.021	**–0.825**	–	0.001	**0.933**	–
	Annual	**0.010**	**–0.461**	–	**0.038**	**0.526**	–
Indus	DJF	0.018	–0.047	0.045	**0.063**	**–0.005**	0.512
	MAM	0.020	–0.091	–0.846	0.030	**0.186**	–0.064
	JJAS	**0.036**	**0.357**	0.494	**0.042**	**0.162**	–0.532
	ON	0.038	0.104	–0.838	–0.016	–0.043	1.730
	Annual	**0.028**	**0.028**	–0.397	**0.036**	**0.079**	0.224
GBM–Delta	DJF	0.009	0.482	–	**0.048**	0.699	–
	MAM	0.001	–0.101	–	**0.089**	–0.127	–
	JJAS	**0.027**	0.186	–	**0.036**	0.725	–
	ON	0.011	–0.501	–	**0.037**	0.800	–
	Annual	**0.010**	0.043	–	**0.043**	**0.712**	–

Table S4. Annual and seasonal trends for NDVI stratified by land cover data for the period between December 2002 and November 2012. All trend values are computed at decadal scale. Bold values represent significant trends (p–value < 0.05).

Basin	Class	DJF	MAM	JJAS	ON	Annual
Ganges	Cropland	**0.062**	**0.015**	0.028	0.009	**0.022**
	Irrigation	**0.050**	**0.015**	**0.034**	–0.001	**0.025**
	Forest	**0.004**	**–0.013**	0.006	0.010	0.005
	Grassland	**0.019**	**0.007**	0.000	0.019	**0.013**
Brahmaputra	Cropland	**–0.028**	–0.028	**0.045**	0.009	–0.010
	Irrigation	–0.010	0.006	**0.077**	0.034	**0.020**
	Forest	–0.029	–0.021	–0.008	0.034	–0.015
	Grassland	0.003	0.005	–0.012	0.011	0.004
Meghna	Cropland	–0.018	0.002	**0.034**	0.006	0.004
	Irrigation	–0.008	0.018	**0.072**	0.044	**0.031**
	Forest	**–0.038**	–0.027	0.009	0.011	–0.009
	Grassland	–0.011	–0.021	0.002	0.022	–0.004
Indus	Cropland	0.014	0.010	0.037	0.011	0.013
	Irrigation	0.008	0.024	**0.045**	0.036	**0.030**
	Forest	0.007	0.015	0.015	0.025	**0.015**
	Grassland	0.008	0.012	0.017	0.022	**0.015**
GBM–Delta	Cropland	–0.009	**–0.036**	0.016	–0.003	–0.006
	Irrigation	**0.020**	0.023	**0.037**	0.014	**0.021**
	Forest	–0.024	–0.018	–0.004	0.013	–0.011
	Grassland	**–0.038**	**0.023**	0.014	–0.019	–0.003

Table S5. Same as Table S3, but for the period between December 2010 and November 2020.

Basin	Class	DJF	MAM	JJAS	ON	Annual
Ganges	Cropland	**0.039**	**0.030**	0.037	0.011	**0.034**
	Irrigation	**0.061**	**0.040**	**0.035**	0.000	**0.037**
	Forest	**0.031**	**0.048**	**0.015**	0.011	**0.023**
	Grassland	**0.024**	**0.025**	0.015	0.019	**0.022**
Brahmaputra	Cropland	**0.071**	**0.096**	–0.009	0.008	**0.040**
	Irrigation	**0.071**	**0.099**	–0.017	0.024	**0.047**
	Forest	**0.039**	**0.042**	0.001	0.000	**0.020**
	Grassland	**0.015**	0.006	0.000	0.017	0.011
Meghna	Cropland	**0.091**	**0.108**	**0.006**	0.005	**0.049**
	Irrigation	**0.095**	**0.065**	**0.019**	0.005	**0.042**
	Forest	**0.058**	**0.083**	–0.007	0.003	**0.031**
	Grassland	**0.045**	**0.051**	–0.006	0.015	**0.030**
Indus	Cropland	**0.043**	**0.027**	0.018	–0.006	**0.023**
	Irrigation	**0.088**	0.022	**0.047**	–0.019	**0.034**
	Forest	**0.036**	**0.050**	**0.027**	–0.013	**0.032**
	Grassland	**0.016**	**0.022**	0.007	–0.008	**0.012**
GBM–Delta	Cropland	**0.024**	**0.108**	**0.048**	0.026	**0.037**
	Irrigation	**0.048**	**0.088**	**0.034**	**0.044**	**0.046**
	Forest	**0.068**	**0.037**	**0.019**	**0.038**	**0.038**
	Grassland	**0.085**	**0.184**	**0.081**	**0.003**	**0.083**

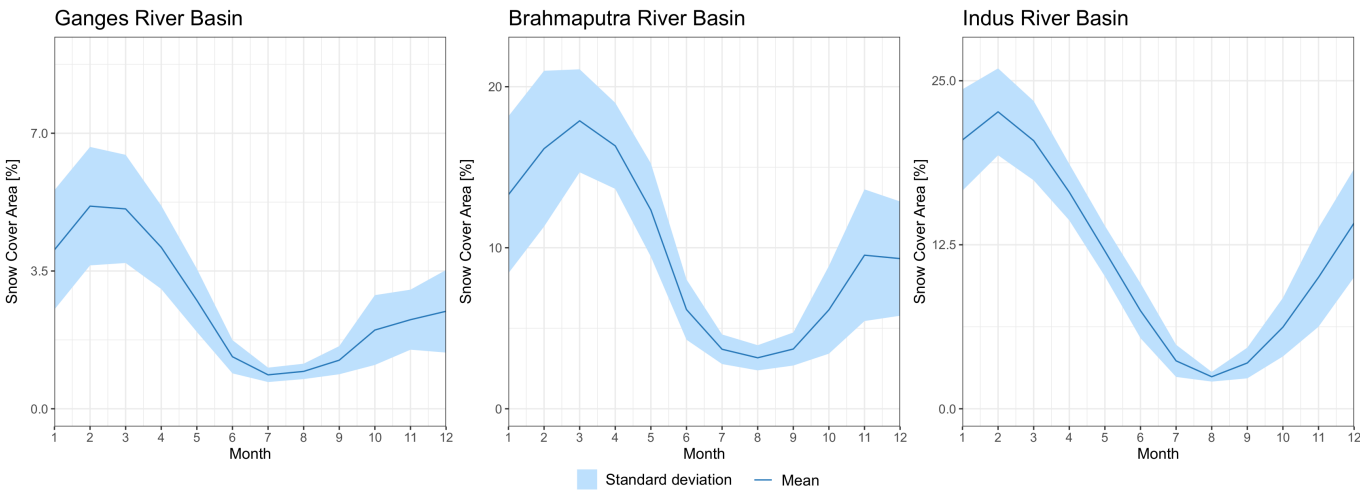

Fig. S8. Seasonality of snow cover area averaged over the studied period.

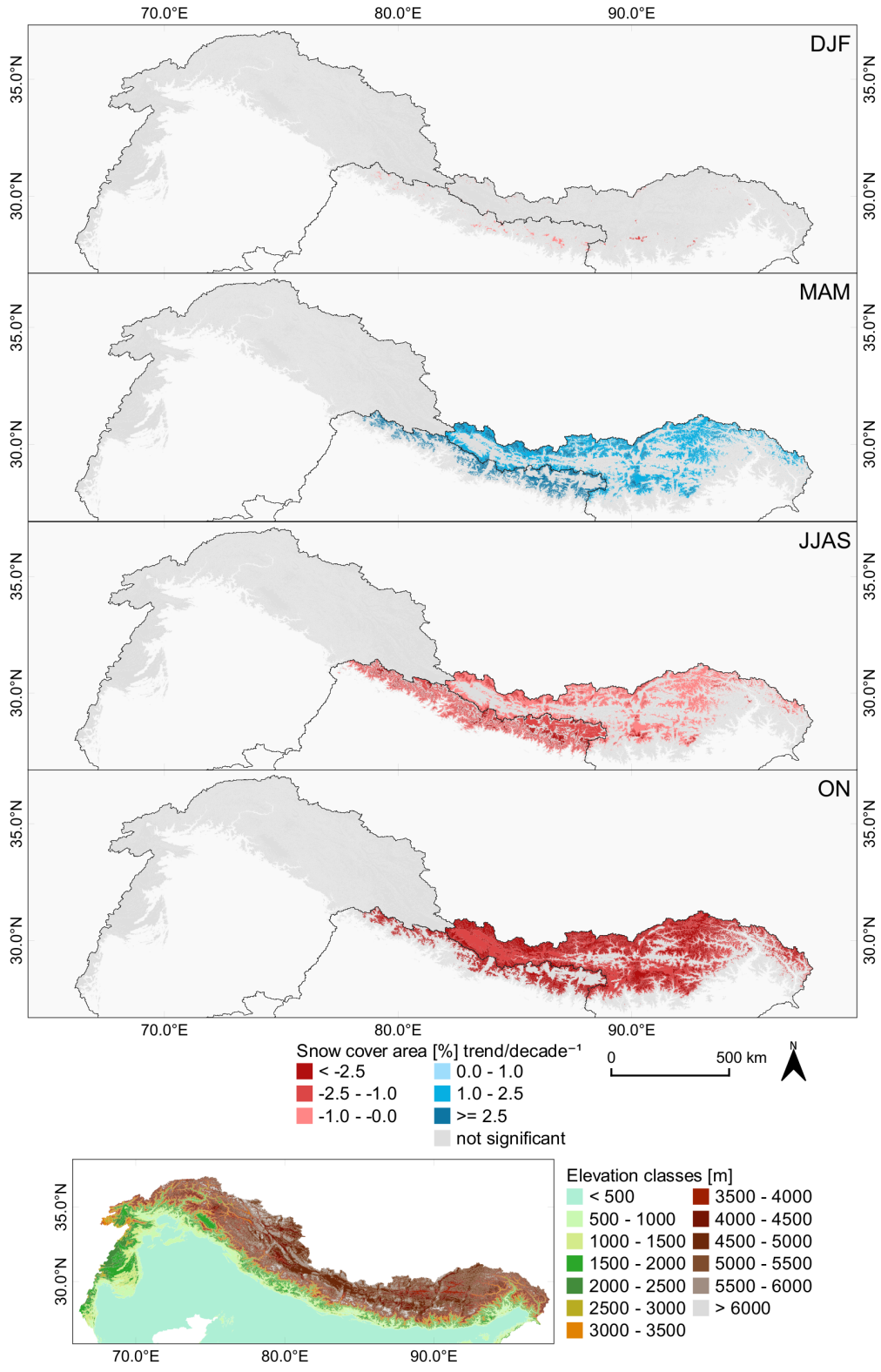

Fig. S9. Seasonal trends for snow cover area aggregated by elevation classes covering the period between December 2002 and November 2020.

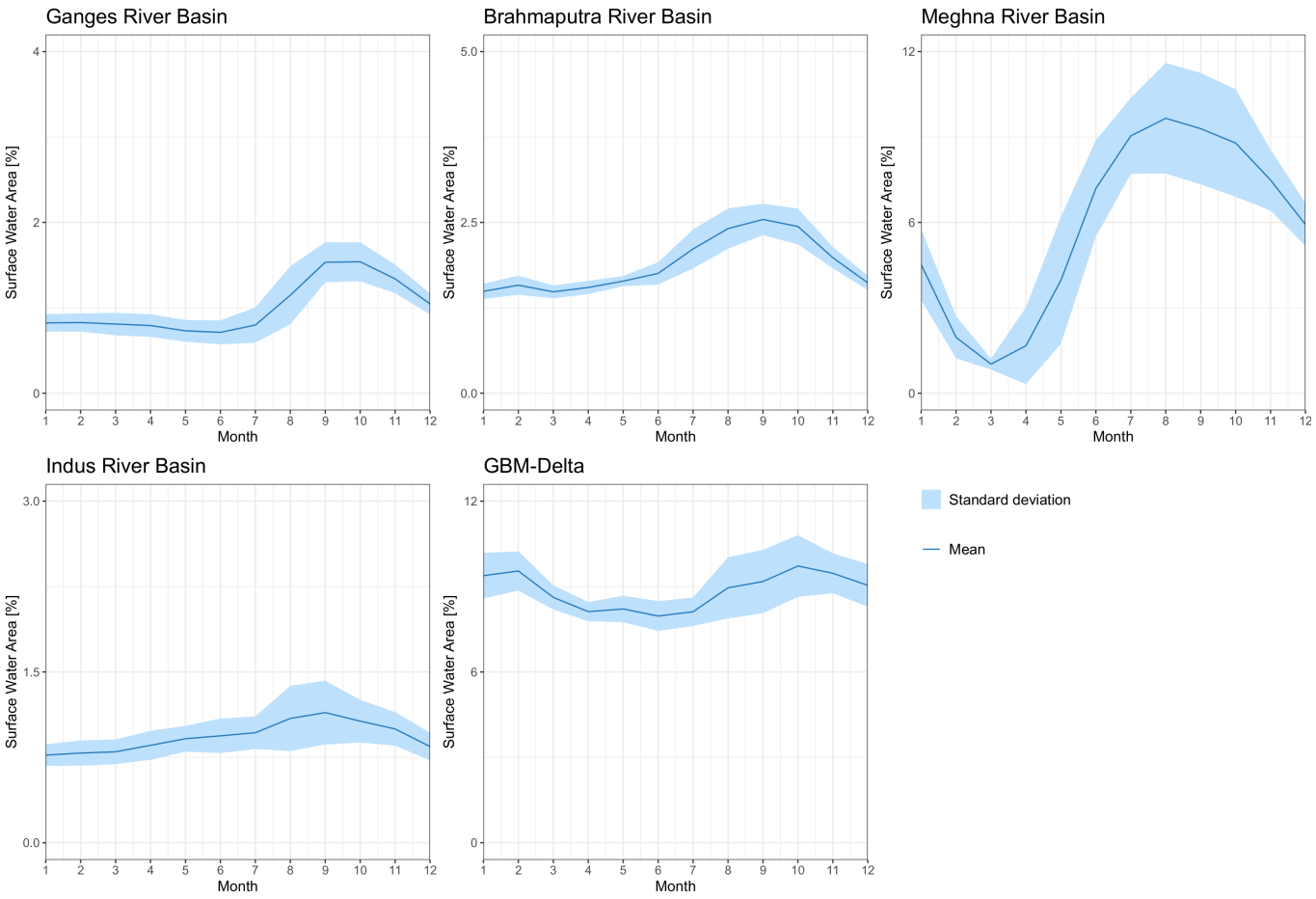

Fig. S10. Seasonality of surface water area averaged over the studied period.

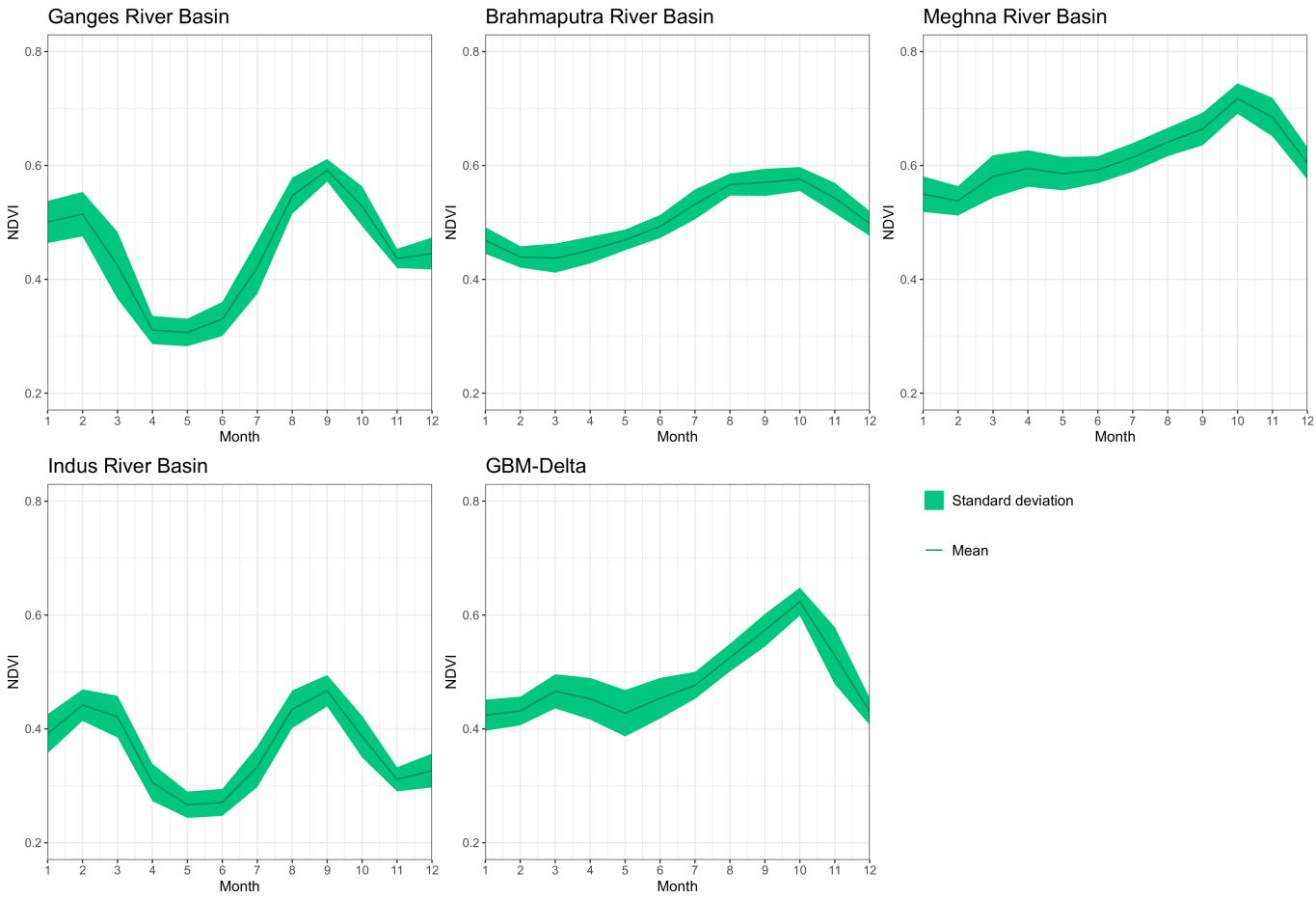

Fig. S11. Seasonality of NDVI averaged over the studied period.